JM PAPERS

Asymptotic coefficients of the attached-eddy model derived from an adiabatic atmosphere

Yue Qin[1] , **Gabriel G. Katul**[2] , **Heping Liu**[3] and **Dan Li**[1,4]

[1]Department of Earth and Environment, Boston University, Boston, MA, USA
[2]Department of Civil and Environmental Engineering, Duke University, Durham, NC, USA
[3]Department of Civil and Environmental Engineering, Washington State University, Pullman, WA, USA
[4]Department of Mechanical Engineering, Boston University, Boston, MA, USA
Corresponding author: Yue Qin, yueqin@bu.edu

The attached-eddy model (AEM) predicts that the mean streamwise velocity and streamwise velocity variance profiles follow a logarithmic shape, while the vertical velocity variance remains invariant with height in the overlap region of high Reynolds number wall-bounded turbulent flows. Moreover, the AEM coefficients are presumed to attain asymptotically constant values at very high Reynolds numbers. Here, the AEM predictions are examined using sonic anemometer measurements in the near-neutral atmospheric surface layer, with a focus on the logarithmic behaviour of the streamwise velocity variance. Utilizing an extensive 210-day dataset collected from a 62 m meteorological tower located in the Eastern Snake River Plain, Idaho, USA, the inertial sublayer is first identified by analysing the measured momentum flux and mean velocity profiles. The logarithmic behaviour of the streamwise velocity variance and the associated '−1' scaling of the streamwise velocity energy spectra are then investigated. The findings indicate that the Townsend–Perry coefficient (A_1) is influenced by mild non-stationarity that manifests itself as a Reynolds number dependence. After excluding non-stationary runs, and requiring the bulk Reynolds number defined using the atmospheric boundary layer height to be larger than 4×10^7, the inferred A_1 converges to values ranging between 1 and 1.25, consistent with laboratory experiments. Furthermore, nine benchmark cases selected through a restrictive quality control reveal a close relation between the '−1' scaling in the streamwise velocity energy spectrum and the logarithmic behaviour of streamwise velocity variance. However, additional data are required to determine whether the plateau value of the pre-multiplied streamwise velocity energy spectrum is identical to A_1.

1. Introduction

The atmospheric surface layer (ASL), typically identified as the bottom 10 % of the atmospheric boundary layer (ABL), extends up to 50–100 m above the ground. It is a layer where the Coriolis effects are minor and may be ignored in the mean momentum balance. Because the air kinematic viscosity ν is small, but typical length and velocity scales associated with turbulence are large, the ASL can serve as a testing ground for assessing asymptotic convergence of laboratory experiments and theories in the limit where similarity coefficients become independent of Reynolds number (Morrison *et al.* 2004; Marusic *et al.* 2010; Marusic & Monty 2019; Hwang *et al.* 2022). However, comparing the ASL to the much studied inertial sublayer (ISL) in canonical turbulent boundary layers of flumes, pipes and wind tunnels is not free from challenges. Unlike laboratory settings where the boundary layer height is often known or controlled, the ABL height varies in time and space and is often not measured. Pragmatic issues such as achieving statistical convergence while ensuring stationarity also arise. The ASL is undoubtedly influenced by diurnal surface heating and cooling, preventing a strict attainment of adiabatic states. Daytime conditions are usually characterized by higher winds but also experience higher surface heating, thereby complicating the full attainment of very large Reynolds numbers in a strict adiabatic manner. Moreover, flow statistics in the ASL are complicated by a plethora of other factors, such as surface heterogeneity, terrain effects and upstream influences, making a zero-pressure gradient condition difficult to ensure (Marusic *et al.* 2010). Despite these difficulties, several observational and comparative studies revealed that the ASL shares some similarities with the ISL of canonical wall-bounded incompressible flows such as zero-pressure gradient boundary layers and fully developed pipe and channel flow (Smits *et al.* 2011; Hutchins *et al.* 2012; Marusic *et al.* 2013; Huang & Katul 2022). Long-term ASL experiments may offer a large ensemble of runs where a subset of those runs permits identifying conditions that match expectations from idealized laboratory studies.

In the ISL of laboratory flows, one of the most widely cited models describing the velocity statistics at very high Reynolds numbers is the attached-eddy model (AEM) (Townsend 1976; Marusic & Monty 2019). For the mean streamwise velocity and streamwise velocity variance, the AEM predicts

$$\frac{\overline{u}}{u_*} = \frac{1}{\kappa} \ln\left(\frac{z-d}{z_0}\right), \tag{1.1}$$

$$\frac{\sigma_u^2}{u_*^2} = B_1 - A_1 \ln\left(\frac{z}{\delta}\right), \tag{1.2}$$

where u is the streamwise velocity component, z is the wall-normal distance with $z = 0$ set at the ground, d is the zero-plane displacement, z_0 is the momentum roughness length, $\sigma_u^2 = \overline{u'^2}$ is the variance of u, where the prime indicates turbulent fluctuations around the mean state, and the overline represents ensemble averaging (often represented by time averaging in the analysis of field data, $u_* = (\tau/\rho)^{1/2}$ is the friction velocity, assumed to be the normalizing velocity for the flow statistics in the AEM, where τ is the wall (or ground) stress defined as $\tau = \mu \ (\partial u/\partial z)|_{z=0}$, μ is the dynamic viscosity of the fluid, ρ is the density of the fluid, and δ is the outer length scale of the flow. The δ value is defined here as the ABL height, which differs from the ASL height or z used in previous work (Kunkel & Marusic 2006; Metzger *et al.* 2007; Marusic *et al.* 2013). These definitional differences translate to higher bulk Reynolds number here when compared to prior work.

The coefficient κ is the von Kármán constant, A_1 is often referred to as the Townsend–Perry coefficient, and B_1 is an empirical coefficient dependent on the flow (i.e. pipe flow versus wind tunnels). Here, κ, A_1 and B_1 are presumed to attain asymptotic constant values at very large Reynolds numbers defined as $Re_\tau = u_* \delta / \nu$ (Marusic *et al.* 2013; Smits *et al.* 2011). For the vertical velocity (w) variance ($\sigma_w^2 = \overline{w'^2}$), the AEM predicts

$$\frac{\sigma_w^2}{u_*^2} = B_2, \tag{1.3}$$

where B_2 is a coefficient that is also expected to reach an asymptotic constant value at very large Re_τ. The logarithmic behaviour of $\overline{u}/u_*$ dates back to work before Townsend (e.g. Prandtl, von Kármán, Izakson and others, as reviewed elsewhere; see Monin & Yaglom 1971), but this is consistent with Townsend's attached-eddy hypothesis and thus is organized here as part of the AEM predictions.

  The work here seeks to examine the applicability of the AEM to the adiabatic ASL with a focus on σ_u^2, which is needed in a plethora of applications, such as footprint modelling and air quality studies (Banta *et al.* 2006; Wyngaard 1988). Additionally, its numerical value is significant to wind energy assessments and to the stability of structures such as towers, bridges and trees (Lumley & Panofsky 1964). There is a growing number of laboratory studies supporting the logarithmic behaviour of σ_u^2 in the ISL (Marusic *et al.* 2010, 2013). However, there have been few studies testing the logarithmic behaviour of σ_u^2 and associated coefficients in the ASL, partly because profiling σ_u^2 in the ASL demands high-fidelity measurements collected at multiple levels and obtaining such data is still challenging. Additionally, links between the logarithmic behaviour of σ_u^2 and the '−1' scaling law in the streamwise velocity energy spectrum did not receive proper attention except in a handful of studies (e.g. Huang & Katul 2022).

  An extensive dataset with turbulence measurements at multiple levels within the ASL is used. These measurements enable a direct evaluation of the logarithmic behaviour of σ_u^2 in the near-neutral ASL, and the inference of A_1 from the profiles of σ_u^2. Before doing this, a brief review of current formulations of σ_u^2 (or streamwise standard deviation σ_u) and the concomitant energy spectrum in turbulent boundary layers, in both atmosphere and laboratory settings, is provided.

1.1. *Magnitude of the turbulent velocity fluctuations*

1.1.1. *Review of ASL formulations for σ_u*

Table 1 summarizes the formulations of σ_u and σ_u^2 found from field experiments in the ASL. According to Monin–Obukhov similarity theory (MOST), the streamwise velocity standard deviations can be expressed as (Obukhov 1946; Monin & Obukhov 1954)

$$\frac{\sigma_u}{u_*} = \phi_u \left(\frac{z - d}{L} \right), \tag{1.4}$$

where L is the Obukhov length measuring the height at which mechanical production of turbulence kinetic energy (TKE) approximately balances buoyancy production or destruction of TKE, whose calculation will be detailed in § 2.4. Here, ϕ_u is a non-dimensional stability function that varies with the stability parameter $(z - d)/L$. Under neutral conditions where $|L| \to \infty$, ϕ_u reduces to

$$\frac{\sigma_u}{u_*} = C_0. \tag{1.5}$$

Sources	Formulations	Fitted constants	Conditions
Lumley & Panofsky (1964)	$\dfrac{\sigma_u^2}{u_*^2} = C_0$	$C_0 = 2.1$–2.9	ASL under near-neutral conditions, pipe flow
Panofsky et al. (1977)	$\dfrac{\sigma_u^2}{u_*^2} = 4 + 0.6\left(\dfrac{\delta}{-L}\right)^{2/3}$		ASL under near-convective conditions, with $-\delta/L$ ranging from 0 to ~ 400
Wilson (2008)	$\dfrac{\sigma_u^2}{u_*^2} = \left[4 + 0.6\left(\dfrac{\delta}{-L}\right)^{2/3}\right]\left[1 - \left(\dfrac{z}{\delta}\right)^{0.38}\right]$		ASL under convective conditions, with $-\delta/L$ ranging from 60 to 1114
Townsend (1976)	$\dfrac{\sigma_u^2}{u_*^2} = B_1 - A_1\ln\left(\dfrac{z}{\delta}\right)$		Attached-eddy hypothesis and dimensional analysis
Perry et al. (1987)	$\dfrac{\sigma_u^2}{u_*^2} = B_1 - A_1\ln\left(\dfrac{z}{\delta}\right) - CRe^{+-1/2}$	$A_1 = 1.03, 1.26$ $B_1 = 2.48, 2.01$ $C = 6.08, 7.50$	Wind tunnel on smooth and rough walls
Perry & Li (1990)	$\dfrac{\sigma_u^2}{u_*^2} = B_1 - A_1\ln\left(\dfrac{z}{\delta}\right) - V[Re^+]$	$A_1 = 1.03, B_1 = 2.39$	Wind tunnel on smooth and rough walls
Marusic et al. (1997)	$\dfrac{\sigma_u^2}{u_*^2} = B_1 - A_1\ln\left(\dfrac{z}{\delta}\right) - V_g\left[Re^+, \dfrac{z}{\delta}\right] - W_g\left[\dfrac{z}{\delta}\right]$	$A_1 = 1.03, B_1 = 2.39$	Wind tunnel at $Re_\tau \sim 734$–$13\,500$ (Marusic & Kunkel 2003), ASL at $Re_\tau \sim 10^6$ with $|z/L| < 0.03$ (Kunkel & Marusic 2006)
Nickels et al. (2007)	$\dfrac{\sigma_u^2}{u_*^2} = B_1 - A_1\ln\left(\dfrac{z}{\delta}\right)$	$A_1 = 1.03, B_1 = 3.65$	Wind tunnel at $Re_\tau \sim 10^4$
Marusic et al. (2013)	$\dfrac{\sigma_u^2}{u_*^2} = B_1 - A_1\ln\left(\dfrac{z}{\delta}\right)$	$A_1 = 1.26, B_1 = 2.3$	Wind tunnel at $Re_\tau = 18\,010$ (Kulandaivelu & Marusic 2010), channel flow at $Re_\tau = 68\,780$ (Winkel et al. 2012)
	$\dfrac{\sigma_u^2}{u_*^2} = B_1 - A_1\ln\left(\dfrac{z}{\delta}\right)$	$A_1 = 1.33, B_1 = 2.14$	Superpipe at $Re_\tau = 98\,190$ (Hultmark et al. 2012), ASL at $Re_\tau \approx 628\,000$ with near-zero heat flux (Hutchins et al. 2012)
Samie et al. (2018)	$\dfrac{\sigma_u^2}{u_*^2} = B_1 - A_1\ln\left(\dfrac{z}{\delta}\right)$	$A_1 = 1.26, B_1 = 1.95$	Wind tunnel at $Re_\tau \sim 6000$–$20\,000$
Huang & Katul (2022)	$\dfrac{\sigma_u^2}{u_*^2} = B_1 - A_1\ln\left(\dfrac{z}{\delta}\right)$	$A_1 = 0.91, B_1 = 2.25$	ASL under neutral conditions at $Re_\tau = 1 \times 10^6$ with $|z/L| \leqslant 0.1$
Hwang et al. (2022)	$\dfrac{\sigma_u^2}{u_*^2} \simeq B_1(Re_\tau) - A_1(Re_\tau)\ln\left(\dfrac{z}{\delta}\right)$	$A_1 \sim 1.01$–1.09	Wind tunnel at $Re_\tau \sim 6123$–$19\,680$

Table 1. A summary of formulations for the normalized streamwise velocity variance. Here, σ_u represents the streamwise velocity standard deviation, σ_u^2 indicates the streamwise velocity variance, z is the height of the sensor, L is the Obukhov length, δ is the boundary layer height, V_g is a viscous correction term that depends on the viscous Reynolds number $Re^+ = zu_*/\nu$, and W_g is a wake correction term. The bulk Reynolds number is defined as $Re_\tau = \delta u_*/\nu$.

Many ASL measurements conducted under near-neutral conditions as well as laboratory flows have been used to fit the empirical parameter C_0. Lumley & Panofsky (1964) surveyed several experiments, and stated that C_0 appears to be independent of z but varies with terrain, with values ranging between 2.1 and 2.9. The survey also noted that under varying stability conditions, vertical and horizontal velocity components exhibit distinct behaviours. While the vertical velocity standard deviation aligns well with MOST predictions, streamwise velocity components are affected differently by $z - d$ and $1/L$. Specifically, a change in z has a negligible effect on streamwise velocity standard deviations, whereas a change in stability (e.g. z/L) has a pronounced effect. A recent study attributed this limitation of MOST to the anisotropy of the Reynolds stress tensor (Stiperski & Calaf 2023).

To account for the 'non-MOST' behaviour of streamwise velocity components and the increase of streamwise wind fluctuations with the deepening of boundary layer height under near-convective conditions, Panofsky *et al.* (1977) proposed an empirical formulation fitted by ASL observations from 30 m to 87 m, with $-\delta/L$ ranging from 0 to ~ 400 given by

$$\frac{\sigma_u^2}{u_*^2} = 4 + 0.6 \left(\frac{\delta}{-L} \right)^{2/3}. \tag{1.6}$$

It should be noted that under neutral conditions, (1.6) is similar to (1.5). This formulation became popular in atmospheric sciences (Wyngaard 1988), although it assumed that changes in z have a negligible effect on σ_u even for near-neutral conditions. Another extensive study was undertaken for unstable conditions with $-\delta/L$ ranging from 60 to 1114 (Wilson 2008) where TKE production and TKE dissipation rates were in approximate balance. These experiments reported a mild z-dependence of the streamwise velocity variance. A refinement to Panofsky's formulation followed, given as

$$\frac{\sigma_u^2}{u_*^2} = \left[4 + 0.6 \left(\frac{\delta}{-L} \right)^{2/3} \right] \left[1 - \left(\frac{z}{\delta} \right)^{0.38} \right]. \tag{1.7}$$

In the near-neutral limit, this expression is reduced to

$$\frac{\sigma_u^2}{u_*^2} = 4 \left[1 - \left(\frac{z}{\delta} \right)^{0.38} \right], \tag{1.8}$$

which confirms that increasing z/δ reduces σ_u^2/u_*^2, as expected from the AEM. Moreover, for very small z/δ, the predicted $\sigma_u/u_* = 2$ agrees with the expected values reported for the ASL (Lumley & Panofsky 1964).

Nonetheless, those developments have been viewed as 'adjustments' to MOST, and have made no apparent contact with the AEM. In fact, after the work of Kaimal (1978), Bradshaw (1978) commented that MOST formulations for the ASL appear to have missed predictions from the AEM about the role of δ in σ_u^2/u_*^2 (Bradshaw 1967), which is briefly reviewed next.

1.1.2. *Townsend's attached-eddy hypothesis*

The AEM postulates that turbulence in wall-bounded flows can be described by a hierarchy of self-similar eddies attached to the wall (Townsend 1976). These eddies are geometrically similar at different scales, with their size proportional to their distance from the wall. Using the equilibrium layer hypothesis where the mechanical production of TKE balances the viscous dissipation, the AEM predicts a specific scaling law in the energy spectrum

(Perry *et al.* 1986; Perry & Li 1990). Further, by integrating the streamwise velocity spectrum across all wavenumbers, σ_u^2 can be formulated as in (1.2) for the overlap region (where the inner region overlaps with the outer region) of turbulent flows. This relation is a cornerstone of the AEM, linking the spectral characteristics of turbulence at a given z to the profile of σ_u^2 (Townsend 1976; Perry & Chong 1982). Meanwhile, the only difference between the smooth and rough walls from the point of view of the Perry & Chong (1982) model is that the smallest hierarchy scales with ν/u_* on smooth walls, while it scales with the roughness length on rough walls.

Since the classic book by Townsend (1976), the AEM has drawn significant experimental and theoretical interest (see table 1). Perry *et al.* (1986) expanded the AEM to include near-wall regions, addressing inner flow dynamics, and providing a theoretical and experimental foundation for the logarithmic law. Subsequently, Perry *et al.* (1987) introduced a $C\,Re^{+-1/2}$ term that depends on the viscous Reynolds number ($Re^+ = zu_*/\nu$) to (1.2) to account for different surface types – smooth, rough and wavy – identifying distinct coefficients (A_1, B_1, C) for each. In a further advancement, Perry & Li (1990) incorporated a viscous correction term $V[Re^+]$, arguing for the formulation's independence from Reynolds number variations, and showing that the constant A_1 is the same on both the smooth and rough walls. Building on these foundations, Marusic *et al.* (1997) proposed a similarity relation to describe the streamwise velocity variance in the logarithmic region, considering inviscid attached eddies and incorporating a viscous correction term $V_g[Re^+, z/\delta]$ in the inner region, and a wake correction term $W_g[z/\delta]$ in the outer region. This formulation was evaluated using wind tunnel and near-neutral ASL data with success.

Metzger *et al.* (2007) tested this similarity formulation using data collected at the Surface Layer Turbulence and Environmental Science Test (SLTEST) facility, confirming the logarithmic behaviour of σ_u^2 in near-neutral ASL conditions. Nickels *et al.* (2007) further explored this formulation by neglecting the correction terms for the viscous and outer flow effects, which were deemed insignificant in their study. These experiments matched well with AEM predictions when setting $A_1 = 1.03$, consistent with the prior value reported in Perry & Li (1990).

Further experimental support for (1.2) was provided by Marusic *et al.* (2013), who analyzed four datasets including boundary layers, pipe flow and ASL measurements with $2 \times 10^4 < Re_\tau < 6 \times 10^5$. Specifically, neutral boundary layer conditions were identified by near-zero heat flux in the ASL dataset (Hutchins *et al.* 2012). Their results not only affirmed the presence of a universal logarithmic region, but also estimated A_1 to be approximately 1.26 for lab flow and 1.33 for ASL data, which is different from the previous estimation $A_1 = 1.03$. They also acknowledged the uncertainties in A_1 estimation arising from the curve-fitting procedure (e.g. ± 0.17 in their ASL dataset). Samie *et al.* (2018) reported $A_1 = 1.26$ based on wind tunnel data within the range $6000 < Re_\tau < 20000$. Similarly, Wang & Zheng (2016) found that their ASL experiments supported the estimate $A_1 = 1.33$, while Huang & Katul (2022) used SLTEST data near the wall (just above the roughness layer) to study the high-order moments of the streamwise velocity, finding a fitted A_1 of approximately 0.9 under near-neutral conditions ($|z/L| \leqslant 0.1$). This value appears to be closer to the value reported by Katul & Chu (1998) for the near-neutral ASL derived from streamwise velocity spectra.

Alongside the variability in A_1, the debate continues regarding the origin of the log law of the streamwise velocity variance. Some studies have employed spectral budget analysis and dimensional analysis, complemented by laboratory experiments (Nikora 1999; Banerjee & Katul 2013), to explain the logarithmic behaviour of streamwise velocity

variance. Recently, Hwang *et al.* (2022) introduced a model inspired by Townsend's original work, addressing the spectrum in the logarithmic layer for various z/δ values. This model suggests that the coefficients A_1 and B_1 depend on the Reynolds number. Their analysis of wind tunnel data at $Re_\tau \sim 6123 - 19\,680$ indicated that the approximated A_1 values vary between 1.01 and 1.09. Furthermore, their model challenges the notion that a '-1' power law in the streamwise energy spectrum is necessary for the logarithmic behaviour in streamwise velocity variance. This evolving understanding underscores the need to verify the universality of the logarithmic behaviour of streamwise velocity variance, particularly within the ASL, and assess to what extent the coefficient A_1 can be derived from the spectrum of the streamwise velocity at a single level z.

1.2. *Streamwise velocity energy spectrum*

In the production range, TKE is generated primarily by the mean shear and 'active' eddies. The streamwise velocity energy spectrum $E_{uu}(k)$ as a function of streamwise wavenumber k in this range typically exhibits a peak corresponding to the energy-containing eddies. In the absence of long-term trends in the record, $E_{uu}(k)$ is expected to level off to a constant value as $k \to 0$ (Kaimal & Finnigan 1994). The AEM argues that in the limit $Re_\tau \to \infty$, and when the wall-normal distance is much smaller than the boundary layer height ($z \ll \delta$), the pre-multiplied power spectral density for $k \sim \mathcal{O}(1/\delta)$ should exhibit a characteristic δ scaling:

$$\frac{k\, E_{uu}(k, z)}{u_*^2} = h_1(k\delta). \tag{1.9a}$$

Similarly, for $k \sim \mathcal{O}(1/z)$, the pre-multiplied power spectral density should follow a z scaling:

$$\frac{k\, E_{uu}(k, z)}{u_*^2} = h_2(kz). \tag{1.9b}$$

In the overlap region where both the outer scaling (δ) and the inner scaling (z) are valid simultaneously ($1/\delta \ll k \ll 1/z$), matching these scaling arguments requires

$$h_1(k\delta) = h_2(kz) = C_1, \tag{1.10}$$

where h_1 and h_2 are two universal functions, and C_1 is a constant independent of both kz and $k\delta$, corresponding to coefficient A_1 in (1.2).

This matching also suggests that in the overlap region (or ISL), the power spectral density must satisfy

$$E_{uu}(k) = C_1 u_*^2 k^{-1}, \tag{1.11}$$

and is independent of z and δ. This spectrum is consistent with the presence of large, energy-containing, self-similar eddies attached to the wall (Bradshaw 1967; Perry & Abell 1977). The k^{-1} power law, originally reported in pipes (Klebanoff 1954), has also been confirmed in many pipe flow experiments since then (Bremhorst & Bullock 1970; Perry & Abell 1975, 1977; Bullock *et al.* 1978).

However, observing a clear k^{-1} scaling in $E_{uu}(k, z)$ is not straightforward. It was already pointed out by Antonia & Raupach (1993) that while the k^{-1} scaling in $E_{uu}(k, z)$ was observed in their high Reynolds number wind tunnel experiments, they precluded its existence in the ASL, citing unavoidable ground (and thermal) inhomogeneity and weak non-stationarity. It was also suggested that the logarithmic layer could be influenced by large-scale motion induced by non-turbulence processes (Wang & Zheng 2016). The

Sources	C_1	Conditions
Pond *et al.* (1966)	1.0	Near-neutral ASL over sea
Turan *et al.* (1987)	0.9, 0.92	Pipes and wind tunnels
Kader & Yaglom (1991)	0.9	Near-neutral ASL
Erm & Joubert (1991)	0.9	Wind tunnel
Antonia & Raupach (1993)	1.0	Wind tunnel experiments over a rough surface
Katul *et al.* (1995)	1.1	Near-neutral ASL over a dry lake bed
Katul & Chu (1998)	1.0	Near-neutral ASL over crops and smooth wall flume
Högström *et al.* (2002)	≈ 1	Neutral ASL over grassy heath
Huang & Katul (2022)	1.01	Near-neutral ASL (SLTEST)

Table 2. A summary of experiments reporting a k^{-1} scaling in the ISL, along with the corresponding C_1 values.

presence of other turbulence structures, such as detached eddies, wake turbulence or other flow irregularities, can contribute to the energy spectrum and obscure the k^{-1} behaviour (Baars & Marusic 2020) that would otherwise be observed in the production range (i.e. the range over which TKE is produced) dominated by attached eddies.

Despite these complexities, several experiments reported a k^{-1} power law in the ASL, with C_1 values ranging from 0.9 to 1.1, as summarized in table 2. Compared to the values in table 1, C_1 determined from fitting $k E_{uu}(k,z)/u_*^2$ tends to be lower than A_1 derived from fitting the profile of σ_u^2. This discrepancy may be attributed to uncertainties in the fitting process and potential misalignment between the x-axis and the incoming wind. Such misalignment could introduce biases from the cross-stream component, thereby reducing the effective production measured (Huang & Katul 2022). However, no study has yet simultaneously obtained and compared both A_1 and C_1 from the same ASL experiments (i.e. very high Reynolds number), which partly motivated the study here.

1.3. *Objectives*

The logarithmic behaviours of the streamwise velocity variance and the k^{-1} scaling in the energy spectra of streamwise velocity in the ASL, as well as their interconnection, are to be explored. Specifically, the following questions are to be addressed.

(i) Can a logarithmic profile of streamwise velocity variance be observed over a flat, homogeneous surface in the adiabatic ASL?
(ii) Using these ASL measurements, what are the dominant factors that influence the variability in A_1?
(iii) Does a k^{-1} scaling regime exist in the energy spectrum of the streamwise velocity in the adiabatic ASL with a plateau value $C_1 = A_1$?

To answer these questions, the paper is organized as follows. Section 2 introduces the field experiment and outlines the data processing and screening methods. Section 3 presents and discusses the results. Section 4 concludes and offers an outlook.

2. Methods

2.1. *Study site*

The study area is located in the Eastern Snake River Plain (ESRP), extending from Twin Falls, Idaho, to the Yellowstone Plateau in the north-east (see figure 1*a*). The
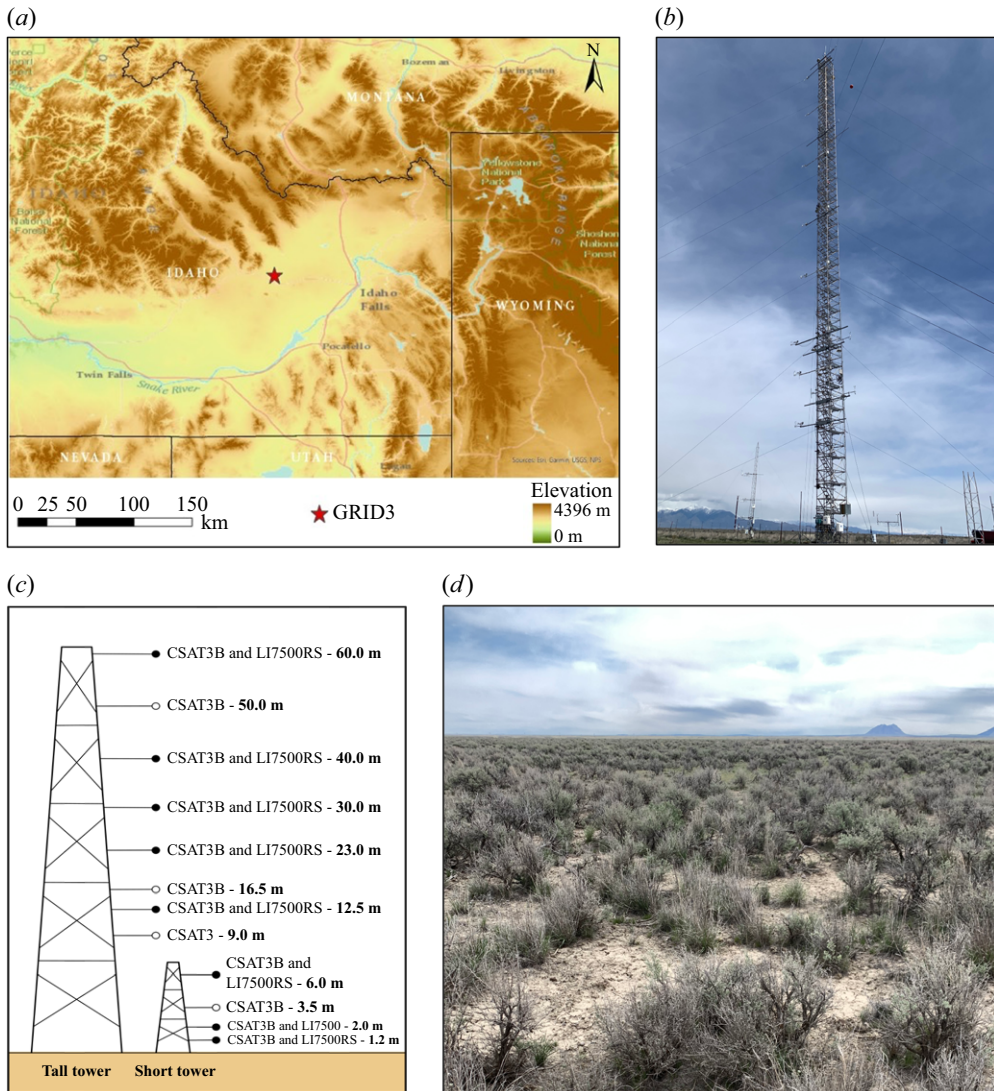
Figure 1. (*a*) Topography of the ESRP, Idaho, USA, based on the 30 m resolution Shuttle Radar Topography Mission (SRTM) dataset (Farr *et al.* 2007). The red star marks the location of the 62 m tower GRID3. (*b*) A photo of the 62 m tower, viewing from the south-east. (*c*) The configuration of the 62 m and 10 m towers. (*d*) Dominant land surface vegetation at the site.

ESRP generally runs in a north-east to south-west direction, and is bordered by large mountain ranges. To the northwest are the Lost River, Lemhi and Bitterroot mountain ranges, which are oriented perpendicularly in a north-west to south-east direction, and rise to approximately 3000 m above mean sea level, approximately 1800 m above the mean elevation of the ESRP. Across the ESRP, the elevation is higher to the north and north-east, and lower to the south and south-west (Clawson *et al.* 2018). This area is commonly influenced by general ESRP downslope winds from the north-east during the night. During the day, this area often experiences synoptic south-westerly winds, and frequent afternoon winds from the south-west that are driven by radiative heating. Under these two prevailing wind conditions, the site has a relatively flat and uniform fetch extending tens

of kilometres upwind (Finn *et al.* 2018*a*,*b*). Additionally, the area experiences shallow nocturnal down-valley winds from the north-west associated with the Big Lost River channel.

2.2. *Field experiments*

The experiment took place at the Idaho National Laboratory (INL) facility (43°35′30″ N, 112°55′50″ W). The general surface of the INL, like that of the entire ESRP, consists of rolling grasslands and sagebrush (see figure 1*d*). Previous work reported that this site is characterized by a zero-plane displacement (d) close to zero, and median z_0 approximately 3 cm for south-west winds and 3.8 cm for north-east winds (Finn *et al.* 2016; Clawson *et al.* 2018). As will be seen later, our estimates of z_0 have a median value of 8 cm during the study period, which extended from 20 September 2020 to 22 April 2021. In this period, 12 measurement levels of eddy-covariance systems were deployed on two towers. The primary measurement site consisted of a 62 m meteorological tower (GRID3) instrumented at eight levels (9, 12.5, 16.5, 23, 30, 40, 50 and 60 m). Additionally, an auxiliary 10 m tower instrumented at four levels (1.2, 2, 3.5 and 6 m) (see figure 1*b*,*c*) was located approximately 15 m away from the GRID3 tower, and the alignment of the two towers was roughly perpendicular to the predominant mean wind direction. Despite the relatively flat and homogeneous surface, this set-up resulted in different measurement footprints between the two towers. The 62 m tower was equipped with retractable square booms (Tower Systems, Inc.) measuring 3.6 m (12 ft), mounted horizontally to provide stable platforms for the sensors. On the 10 m tower, 1.8 m (6 ft) poles were used, ensuring that the sensors were placed approximately 1.5 m away from the tower's structure.

The eddy-covariance systems used in the experiment included two models of triaxial sonic anemometers (CSAT3B and CSAT3, Campbell Scientific, Inc.), and two models of infrared gas analysers (IRGAs; LI7500RS and LI7500, LICOR, Inc.). The sonic anemometers measured the velocity components along the north–south, east–west and vertical directions, respectively, relative to the reference frame fixed to the sonic anemometer. Sonic azimuth was estimated by comparing the calculated and measured wind directions from sonics and wind vanes. The sonic anemometers were oriented slightly towards the north-north-west, rather than directly north. The IRGAs measured the densities of water vapour and CO_2. The sampling frequency was 10 Hz for all anemometers. The CSAT3s had vertical sonic paths of 10 cm and horizontal paths of 5.8 cm, operating in a pulsed acoustic mode. Corrections for the effects of humidity and density fluctuations on the turbulent fluctuations of sonic temperature and the densities of water vapour and CO_2 have been detailed elsewhere (Gao *et al.* 2024). These scalar measurements are needed only to estimate whether L is sufficiently large and thus whether the flow is near neutral.

2.3. *Data processing*

Data processing involves coordinate rotation, detrending and neutral case screening. High-frequency spectral corrections are neglected because the contribution from the high-frequency region to turbulence intensity is small. For example, the data indicate that the errors caused by path averaging are 2–3 orders of magnitude smaller than the streamwise velocity variance (σ_u^2).

2.3.1. *Averaging period*

In the analysis of ASL data, fluctuations with periods less than approximately one hour are generally considered turbulence, while slower fluctuations are synoptic-scale and treated

1011 A29-10

as part of the mean flow (Wyngaard 1992). Consequently, a one-hour averaging period is selected as a compromise between the need to resolve large eddies reliably and stationarity considerations. However, Metzger *et al.* (2007) suggested that the neutral periods are often short, of the order of several minutes. Previous studies have used various averaging periods depending on the stability and conditions of the boundary layer. For instance, 10 min was used in the stable boundary layer in the CASES-99 experiment (Banta *et al.* 2006), 30 min in the unstable conditions when mechanical production of TKE was compared to viscous dissipation (Wilson 2008), 20 min in neutral conditions in the SLTEST experiment (Metzger *et al.* 2007), and 1 hour in neutral conditions in the same SLTEST experiment (Hutchins *et al.* 2012). Additionally, 30 min was used in SLTEST (Huang & Katul 2022), 15 min in the unstable LATEX experiment (Li & Bou-Zeid 2011), and 1 min for stable and 30 min for unstable conditions across 13 datasets (Stiperski & Calaf 2023).

A shorter sampling period, while increasing steadiness in mean meteorological conditions, can also affect statistical convergence by reducing sample size, increasing sensitivity to outliers, and potentially biasing the representative nature of the data. In general, the difference between ensemble averaging (the sought quantity) and time averaging is labelled as systematic bias. This bias declines with reduced $2T_L/T_p$ (Lenschow *et al.* 1994), where T_L is the integral time scale of a flow variable, and T_p is the averaging period. Typical T_L values for the streamwise velocity are of the order of 1–2 min, hence selecting $T_p = 60$ min is acceptable for reducing the systematic bias.

A comparison between 1 hour and 30 min averaging periods is also conducted to assess the sensitivity of the results to the choice of averaging window. The results suggest that the 30 min averaging period only increases the variability in the fitted coefficients, while the overall conclusions of this study remain unaltered. Therefore, the 1 hour averaging period is considered a more suitable choice for the analysis, striking a balance between reducing systematic bias and maintaining statistical robustness.

2.3.2. *Coordinate rotation*

Assuming that the sonic anemometers are nearly level, requiring only minor tilt corrections to align the vertical axis perpendicular to the mean flow, the double rotation method (Wilczak *et al.* 2001) involves two sequential rotations: first, a pitch rotation to set the mean vertical velocity component ($\overline{w}$) to zero; and second, a yaw rotation to set the mean lateral velocity component ($\overline{v}$) to zero. Given the relatively flat and homogeneous terrain, this standard method is initially applied to correct the tilt of the anemometers.

Another commonly used rotation procedure in micrometeorology is the planar fit method (Wilczak *et al.* 2001; Aubinet *et al.* 2012), which is particularly suited for complex terrain where a non-zero mean vertical velocity may exist. To evaluate whether the fitted coefficients in the AEM are sensitive to different coordinate rotation methods, this study applies the planar fit method. The data are first grouped into six wind direction sectors at 60° intervals, then a plane is fitted to all the data within each sector over the entire seven-month experimental period.

2.3.3. *Detrending*

After the coordinate rotation, the time series in figure 2(*a*) shows a superposition of the high-frequency turbulent fluctuations and low-frequency oscillations. Detrending is employed to remove long-term trends or patterns in the data, which can result from various factors, such as instrument drift and atmospheric changes (Moncrieff *et al.* 2004). By removing the low-frequency content, the analysis can focus on short-term variability (i.e. turbulence) and ensure a certain amount of stationarity.
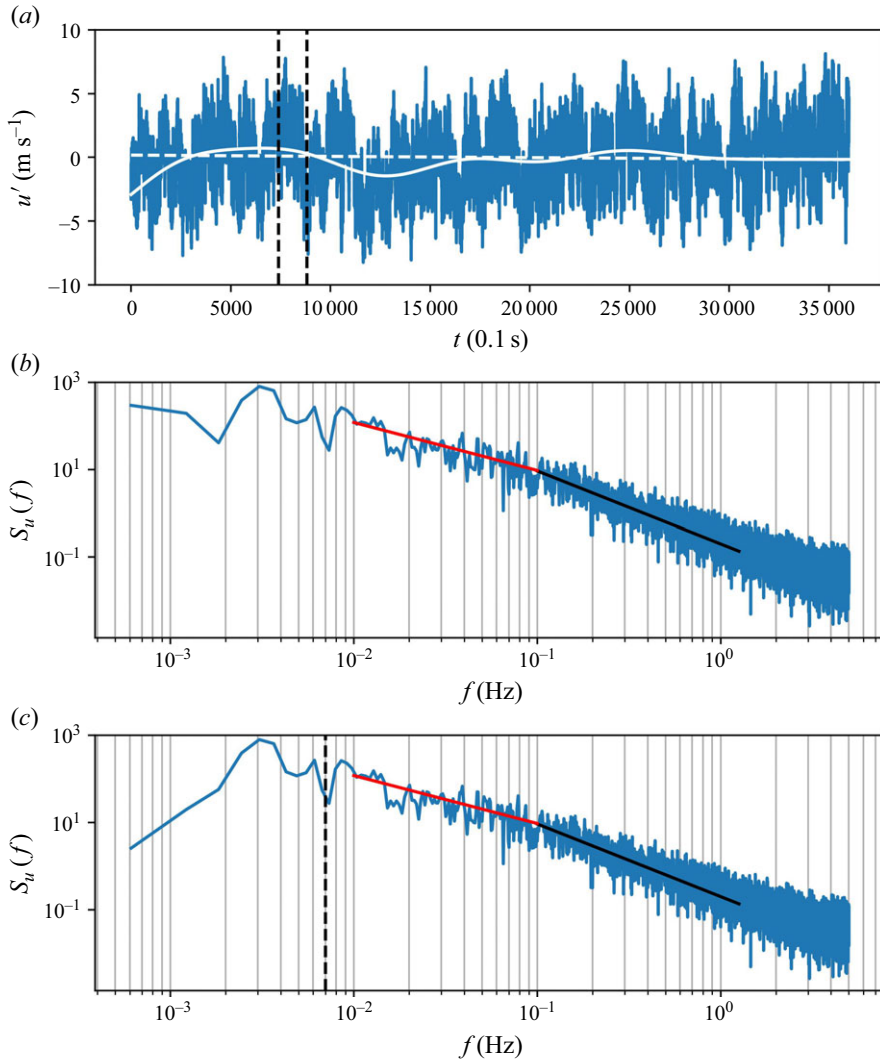
Figure 2. Streamwise velocity time series, u, sampled at 10 Hz from the triaxial sonic anemometer at 12.5 m on 25 September 2020, at 15:00 local time (LT). (a) Turbulent component of streamwise velocity after coordinate rotation: the dashed white line shows the linear fit, the solid white line represents high-pass filtered low-frequency signals that are nonlinear, and the vertical dashed black lines mark the filter size for the high-pass method. (b) Energy spectrum of u after linear detrending: the solid red line and solid black line represent f^{-1} and $f^{-5/3}$ scalings, respectively. (c) The energy spectrum of u after high-pass filtering: the vertical dashed black line indicates the cut-off frequency corresponding to a 2000 m wavelength, for which the filter size is 142 s.

A common method in micrometeorology is linear detrending, where the line of best fit over the averaging period (dashed white line in figure 2a) is subtracted from the original time series. While primarily affecting the low-frequency part of the signal, linear detrending can impact all frequencies and introduce oscillations at higher frequencies (Moncrieff *et al.* 2004).

Alternatively, high-pass filtering can isolate low-frequency signals by convolving the original data with a transfer function in the frequency domain, a method often used in post-processing (Nickels *et al.* 2005; Metzger *et al.* 2007; Hutchins *et al.* 2012). However,

determining a clear cut-off frequency to separate turbulent motions from long-term trends is challenging, posing a risk of filtering out low-wavenumber turbulent motions. A tenth-order Butterworth filter is applied in this work, with a cut-off frequency equivalent to a 2000 m cut-off wavelength. It translates to filter size 100–350 s that varies with mean wind speed at different levels. Those sizes align closely with the observed time period of low-frequency signals in the time series (indicated by the two vertical lines in figure 2*a*). This filter size is consistent with previous turbulent boundary layer studies that selected 180 s in Hutchins *et al.* (2012) and 181.8 s in Puccioni *et al.* (2023).

As shown in figure 2(*b*), the linear detrended streamwise velocity energy spectrum $S_u(f)$ levels off as $f \to 0$. In contrast, the high-pass filtered $S_u(f)$ shows more removal of low-frequency content (very-large-scale motions) than linear detrending, with a much faster decay as $f \to 0$, as expected (see figure 2*c*). Nevertheless, the best method depends on site conditions. Therefore, both methods are initially applied, and a comparison is performed to ensure the derived AEM coefficients are not sensitive to the detrending approach.

2.3.4. *Turbulence statistics*

After detrending, time averaging of all instantaneous data is conducted to obtain first the mean component and then the turbulent fluctuations as $u' = u - \overline{u}$, $v' = v - \overline{v}$, $w' = w - \overline{w}$ and $T' = T - \overline{T}$, where T is the air temperature. The Reynolds stress methods and profile methods are two conventional approaches to estimating the friction velocity in the ASL and those two methods will also be compared for reference.

(i) Reynolds stress method. In an ideal ASL that is high Reynolds number, stationary, planar homogeneous, lacking subsidence and characterized by a zero mean pressure gradient, the momentum fluxes must be invariant to variations in z. To test the constant flux layer assumption and determine u_* to be used as a normalizing velocity in the AEM, a local friction velocity is defined as

$$u_* = \left[\overline{u'w'}^2 + \overline{v'w'}^2 \right]^{1/4}. \tag{2.1}$$

(ii) Profile method. Another approach to estimating u_* is based on the logarithmic law of the mean velocity as shown in (1.1). This technique, known as the Clauser chart method (Clauser 1956), is commonly used by boundary layer experimentalists. Measurements of the mean velocity profile can be used to estimate the friction velocity by fitting the measured $\overline{u}$ against $\ln(z)$. To do so, it is necessary to identify the beginning and ending points that follow a log-linear relation, which can involve some subjectivity. The magnitude of the friction velocity is directly related to the choice of the von Kármán constant (Kendall & Koochesfahani 2008).

Agreement between these two methods is also used when identifying the span of the ASL.

2.4. *Data selection*

From the 210 days of data recorded, the focus is placed on a subset that is approximately neutrally stratified. The stability of the surface layer is characterized by the stability parameter $|z/L|$, where near-neutral conditions are defined as $|z/L| < 0.1$. The local Obukhov length L is calculated as $L = -\overline{T}u_*^3/(\kappa g \, \overline{w'T'})$, where g is the gravitational acceleration, and the time-averaged sonic temperature $\overline{T}$ is assumed to be a good approximation to the virtual temperature θ_v. Since multiple measurement levels are
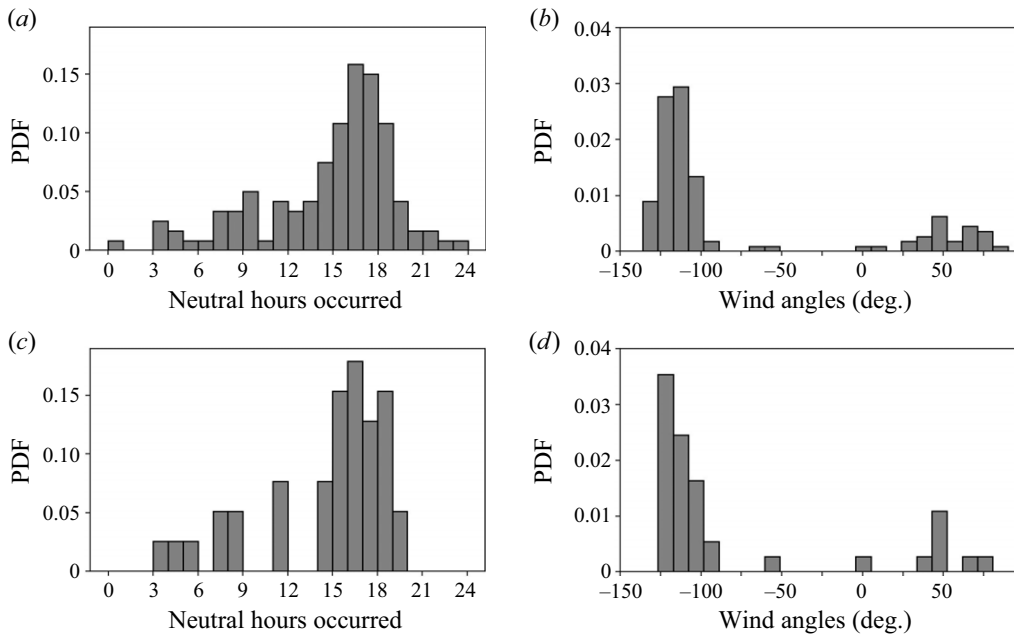
Figure 3. The PDFs of the 120 near-neutral cases (*a*) by time of day, and (*b*) by wind angles, at 16.5 m relative to true north, with positive values denoting clockwise, negative values anticlockwise, and 0 denoting northerly wind. Neutral conditions are identified during hours when $|z_{mean}/L_{median}| < 0.1$ is satisfied. The PDFs of the 39 post-screening near-neutral cases: (*c*) by time of day, and (*d*) by wind angles. Here, (*c*) and (*d*) are shown to facilitate comparisons before and after data quality control, with the data quality control discussed in detail in § 3.2.2.

considered, the stability parameter is calculated as z_{mean}/L_{median}, where z_{mean} is the geometric mean of the sensor heights, and L_{median} is the median value of the local Obukhov length L across the considered levels. This choice of using the median Obukhov length (L_{median}) and the geometric mean of sensor heights (z_{mean}) is consistent with the methodology outlined in Andreas *et al.* (2006). This step results in 142 cases remaining. The following criteria are used for further data selection to be consistent with previous ASL studies (Li & Bou-Zeid 2011).

(i) Wind must face the sonic anemometers. The angles between the time-mean wind direction and the sonic anemometers have to be smaller than 120° such that the interference and data contamination from the anemometer arms, tripods and other supporting structures are minimized, which further narrows down the runs to 139.

(ii) The turbulence intensity ($\sigma_u/\overline{u}$) must be less than 0.5 to justify the use of Taylor's frozen turbulence hypothesis (Taylor 1938), leading to 134 cases remaining.

After applying the above screening procedures and removing cases with pressure measurement errors associated with the gas analyser, 120 cases are retained for further analysis. Figure 3(*a*) illustrates the probability density function (PDF) of near-neutral conditions, showing that a neutrally stratified ASL can occur throughout the day, peaking at approximately 16:00 LT. The wind is consistently dominated by a west-south-westerly wind direction (as shown in figure 3*b*), with few instances of wind from the east-north-east, likely occurring at night.
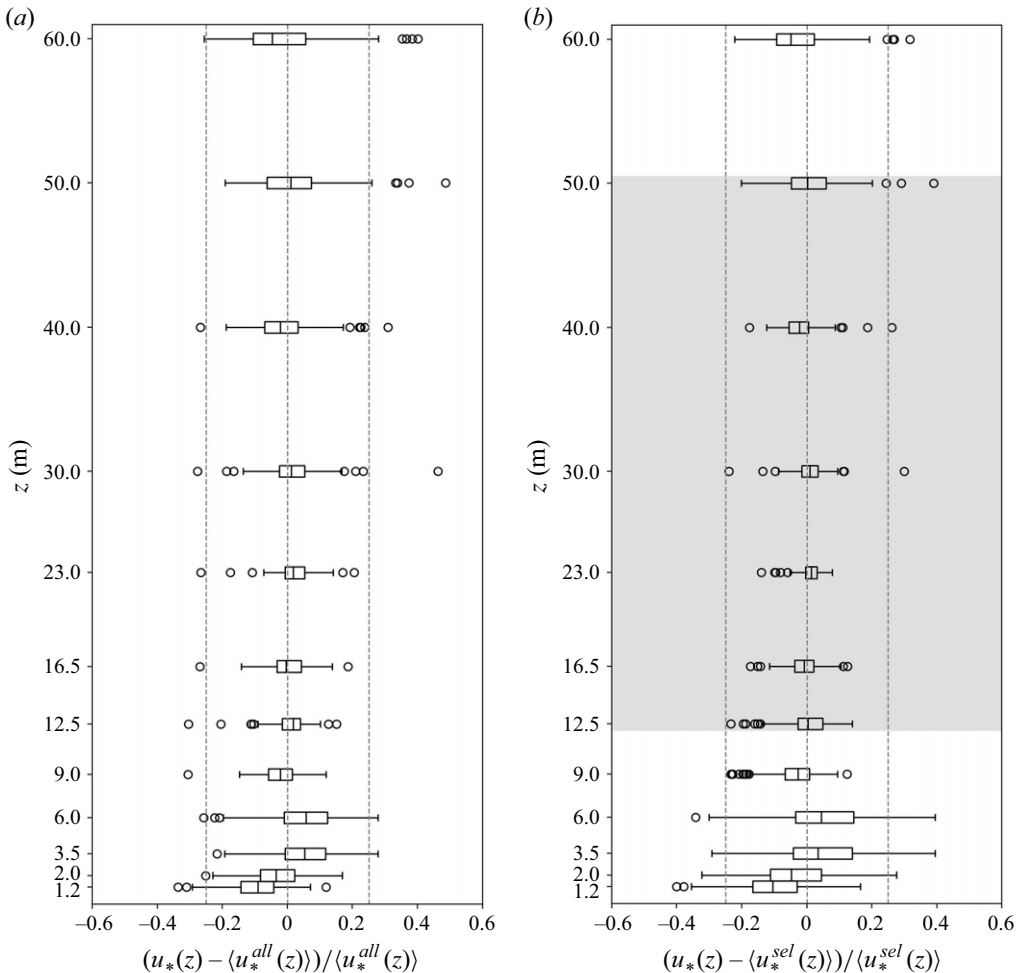
Figure 4. Deviation of locally measured friction velocity from the vertical mean averaged across (*a*) all twelve levels and (*b*) the six levels within the ISL for the linear detrended measurements. Box plot interpretation: from left to right, lines signify the minimum, first quartile, median, third quartile and maximum values. Black open circles denote outliers. Vertical dashed lines are set at $-0.25, 0, 0.25$. The grey shaded region highlights the ISL identified between 12.5 m and 50 m, which is the operational range used in evaluating the AEM. The terms $\langle u_*^{all}(z) \rangle$ and $\langle u_*^{sel}(z) \rangle$ represent the friction velocities averaged over all twelve levels and the six shaded levels, respectively.

3. Results

3.1. *Determination of the ISL*

The local friction velocity computed using (2.1) is investigated first. Figure 4(*a*) illustrates the vertical distribution of local $u_*(z)$ and their deviations from the vertical average across all 12 levels ($\langle u_*^{all}(z) \rangle$, where the angle brackets indicate vertical average). Notably, the friction velocity at the lowermost four levels exhibits significant deviations from the vertical average with increasing trend in z. Three potential explanations are considered for this observation. First, the lower four levels are mounted on a separate 10 m tower, located approximately 10 m from the 62 m tower, as shown in figure 1(*b*). Despite the flat and aerodynamically homogeneous surface cover, variations in tower placement may influence turbulent momentum flux measurements near the ground. Second, although the
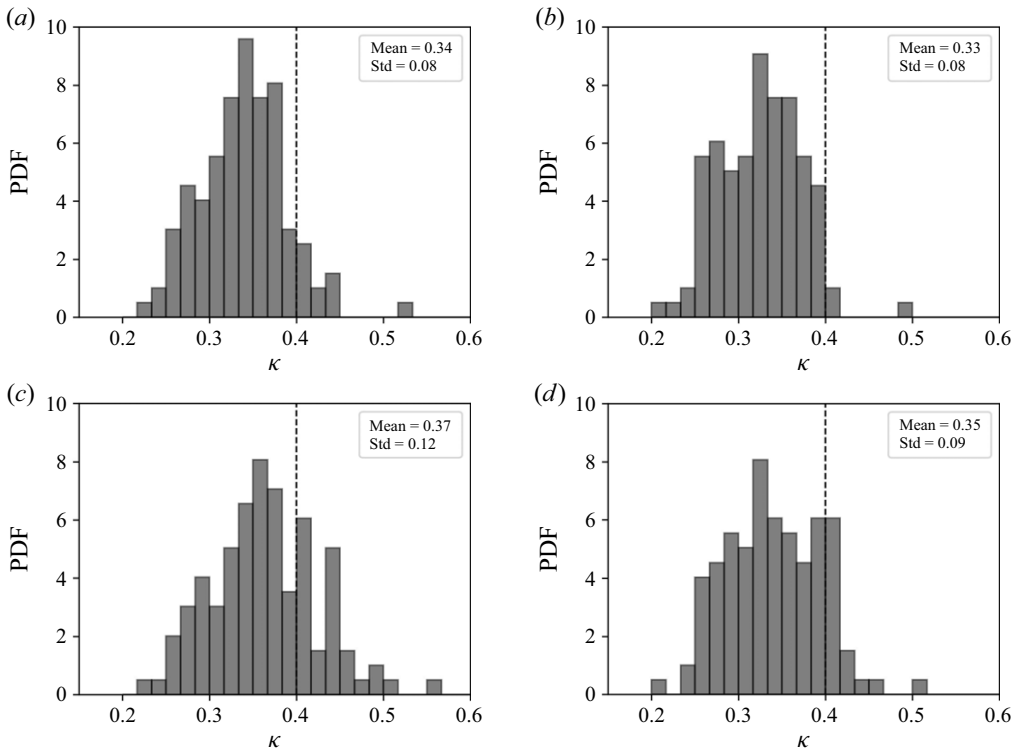
Figure 5. The PDFs for the inferred κ values using the mean horizontal velocity from the following levels: (*a*) 9–50 m, (*b*) 9–60 m, (*c*) 12.5–50 m, (*d*) 12.5–60 m. Vertical dashed lines indicate $\kappa = 0.4$. The computed means and standard deviations of the fitted κ are shown.

sagebrush is relatively short (tens of centimetres) and the lowest anemometer level is at 1.2 m, the z_0 value derived from the log mean profile has median value approximately 0.08 m. According to Garrett (1994), the roughness sublayer's height can be 10–150 times z_0. Assuming a factor of 100 times the roughness length (i.e. 7 m), the roughness sublayer would extend just above the 6 m level. Finally, volume averaging by the sonic anemometer path length (10–15 cm) has a disproportionate impact on the vertical velocity at levels close to the ground, leading to an underestimation of the covariance (and thus friction velocity) at those levels. Therefore, the analysis here excludes the bottom four levels when defining the ISL.

The remaining eight levels, from 9 m to 60 m, show consistent local u_* vertical distribution. To test whether all these eight levels are within the ISL, (1.1) is further applied to fit a friction velocity u_*^{fit}, assuming $\kappa = 0.4$. The u_*^{fit} value is consistently 10–20 % higher than the local $u_*(z)$ at these eight levels, implying that the measured turbulent momentum flux and mean velocity at these levels are not entirely consistent with a logarithmic mean velocity profile with $\kappa = 0.4$.

To identify data consistent with a logarithmic mean velocity profile with κ close to 0.4, the local u_* is used to fit κ. Using the remaining eight levels (ranging from 9 m to 60 m), four scenarios for fitting κ are tested: (*a*) using data from 9 m to 50 m; (*b*) using data from 9 m to 60 m; (*c*) using data from 12.5 m to 50 m; and (*d*) using data from 12.5 m to 60 m. The PDFs of the inferred κ values are shown in figure 5 for all these scenarios. The results indicate that only when using data from 12.5 m to 50 m does the fitted κ have mean close to 0.4 and exhibit a quasi-Gaussian distribution in the spread, while other scenarios produce
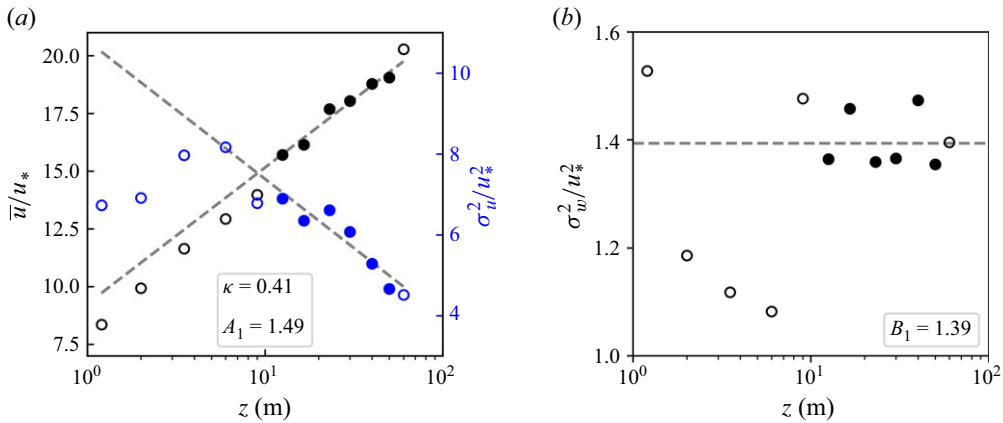
Figure 6. Fitting κ, A_1 and B_2 with high-pass filtered data on 25 September 2020, at 15:00 LT: (*a*) the mean velocity profile (in black), and the streamwise velocity variance profile (in blue); (*b*) the vertical velocity variance profile. Closed circles indicate the selected data within the ISL. Dashed grey lines denote the linear regression based on the selected data within the ISL. Insets show the results of the fitting.

κ values that either deviate largely from 0.4 or do not follow a Gaussian distribution in their spread. The same analysis performed on high-pass filtered data produces results similar to those from the linearly detrended data, and are thus not presented.

Based on this analysis of local u_*, the data between 12.5 m and 50 m are selected for further analysis of the AEM, and this range is treated as the ISL (with the deviation of the locally measured u_* from their vertical average shown in figure 4*b*). The friction velocity used for normalization in the following analysis is the vertically averaged friction velocity across this range ($\langle u_*^{sel}(z) \rangle$).

3.2. *Magnitude of the turbulent velocity fluctuations*

3.2.1. *Estimation of κ, A_1 and B_2 in the ASL*

With u_* and σ_u^2 within the ISL measured, a linear regression is conducted to derive the values of A_1 by fitting σ_u^2 to $\ln(z)$ utilizing (1.2). Notably, this fitting method for obtaining A_1 does not require direct measurement of δ, but cannot be used to infer the B_1 constant of the AEM. Figure 6(*a*) demonstrates one such linear regression for the hour 15:00 LT on 25 September 2020, detrended by high-pass filtering. Note that only the closed circles are used for regression because they are situated in the ISL. The logarithmic mean velocity profile is also shown for comparison. The results indicate that the fitted κ ($= 0.41$) is very close to the accepted 0.4 value. Moreover, the σ_u^2 profile aligns with AEM predictions, confirming the logarithmic dependence on z of streamwise velocity variance within the ISL (highlighted by closed circles) at a very high Reynolds number.

To estimate B_2 in (1.3), σ_w^2 is fitted against the local u_*^2 within the ISL, and the resulting slope is retrieved. For example, a B_2 value 1.39 is obtained for the hour 15:00 LT on 25 September 2020, as can be seen from figure 6(*b*). While similar values for B_2 (i.e. approximately 1.4) have been observed in the ASL literature (Yang & Bo 2018), they are lower than the theoretically predicted value 1.65 for an idealized infinite Reynolds number case. The value 1.65 can be obtained by considering the vertical velocity energy spectrum $E_{ww}(k)$, which consists of a flat energy-containing region spanning wavenumbers from $k = 0$ to $k = k_a$ (energy splashing region) and an inertial subrange from $k = k_a$ to $k = \infty$, where $k_a = (kz)^{-1}$ represents the transition wavenumber. Assuming a balance between TKE production and dissipation, the normalized vertical velocity

| | κ | | | A_1 | | | B_2 | | |
	I	II	III	I	II	III	I	II	III
Mean	0.38	0.37	0.38	0.18	1.25	1.22	1.37	1.45	1.40
Std	0.07	0.12	0.05	1.50	0.84	0.33	0.22	0.18	0.11
Mean	0.39	0.37	0.38	0.33	1.15	1.24	1.31	1.43	1.40
Std	0.08	0.07	0.04	1.24	0.82	0.39	0.25	0.19	0.11

Table 3. Comparison of the fitted values of the von Kármán constant (κ), AEM coefficient (A_1) and B_2 between group I (linear-detrended data), group II (high-pass filtered data), and group III (high-pass filtered data with $Re_\tau > 4 \times 10^7$ and $R^2 > 0.6$). Here, B_2 is estimated from the slope of σ_w^2 over u_*^2 within the ISL. The R^2 values represent the coefficients of determination of the fits. The first two rows display results from double rotation, while the bottom two rows are from planar fit.

variance is given by $(\sigma_w/u_*)^2 = (5/2)C_{o,w}$, with $C_{o,w} = 0.65$ as the Kolmogorov constant for the one-dimensional vertical velocity spectrum in the inertial subrange. Thus for such an idealized case, this relation predicts $B_2 = 1.65$. In the area calculation of E_{ww}, $(3/2)C_{o,w}$ out of the total $(5/2)C_{o,w}$ originates from extending the inertial subrange from $k = k_a$ to $k = \infty$, while the remaining $C_{o,w}$ comes from the large eddies (i.e. those with scales larger than $1/k_a$). Therefore, the reduced B_2 observed here can potentially be attributed to sampling limitations. Specifically, the 10 Hz sampling frequency and path-averaging effects of the anemometer may disproportionately under-resolve the inertial subrange components of the vertical velocity (w) compared to its longitudinal (u) counterpart.

To assess the consistency of the logarithmic behaviour of the streamwise velocity and associated AEM coefficients in the near-neutral ASL, the same fitting procedures are applied across all 120 neutral cases. The goodness of fit for (1.1)–(1.3) is quantified using the coefficients of determination (R^2). The comparison of the results between linearly detrended data and high-pass filtered data can be found in table 3. Note that the linear detrending method and the high-pass filtering method give different $\overline{u}$, u_* and σ_u. The analysis shows that the mean estimated values of κ for both methods are similar, yet smaller than 0.4. This result aligns with previous experiments (Andreas *et al.* 2006; Marusic *et al.* 2010) and theoretical predictions based on the co-spectral budget (Katul *et al.* 2013), where κ is linked to the Rotta constant – an isotropization parameter associated with rapid distortion theory – and the Kolmogorov constant. However, the fitted values of κ exhibit substantial variability. Such variability is not uncommon since extensive evidence suggests that κ is not a universal constant but rather depends on flow conditions even for weak (in)stability effects (Österlund *et al.* 2000; Andreas *et al.* 2006; Nagib & Chauhan 2008). Furthermore, the fitted B_2 are relatively consistent between two detrending methods. As a result, the current analysis focuses on A_1. The high-pass filtered data exhibit a more robust logarithmic scaling of σ_u^2 than the linearly detrended data. This outcome is based on the finding that the linear detrending method yields a wider range of R^2 values, with average 0.67 and standard deviation 0.32. In contrast, the high-pass filtering yields a higher mean (0.81) and a lower standard deviation (0.23) in R^2 scores. Moreover, the derived A_1 values of linear-detrended data exhibit significant variability, often departing considerably from the conventional range 1–1.3, and frequently resulting in negative A_1 values (31.63 % and 9.18 % negative occurrence for linear detrending and high-pass filtering, respectively). The potential reasons for this deviation are discussed next.

Given an averaging period of 1 hour, the turbulence data might experience unsteadiness associated with larger-scale meteorological influences such as static pressure gradients.

According to Högström *et al.* (2002), 'inactive' turbulence becomes more significant as the pressure gradient increases, potentially obscuring the scaling behaviour predicted by the AEM. While the linear-detrending method only removes the mean trend, it might not sufficiently eliminate the (nonlinear) large-scale meteorological influences, potentially leading to negative fitted values of A_1. This underscores the importance of removing larger-scale meteorological influences in ASL data when comparing them to a canonical turbulent boundary layer. Furthermore, sensitivity tests indicate that the fitting outcomes are not sensitive to the choice of the cut-off frequency in the 100–200 s range for the high-pass filtering method. Consequently, the following analysis focuses on high-pass filtered data.

Finally, table 3 presents results from both the double rotation and planar fit methods, showing essentially no differences in the fitted κ values. The fitted A_1 and B_1 differ between the two methods. However, as will be seen in § 3.2.2, once data quality control is applied, the difference between the double rotation and planar fit methods becomes much smaller even for fitted A_1. As such, the following discussion is based primarily on the double rotation method.

3.2.2. *Objective data quality control*

To understand the variations in the fitted A_1, key factors that influence data quality are investigated, including statistical fitting performance, non-stationarity effects, the presence of a constant σ_w with height in the ISL, and the Reynolds number effect. Other effects, such as wind turning with height and wind shear, are shown to be very small and are thus not considered.

(i) Fitting performance. Before discussing the fitted coefficients of the AEM to the data here, it is necessary to evaluate the goodness of the logarithmic scaling for σ_u^2. The coefficient of determination (R^2) from the logarithmic fitting is examined, and anomalous cases less than a threshold are filtered out to ensure that only high-quality fits are considered when evaluating A_1.

(ii) Non-stationarity effects. Stationarity is a necessary condition for the AEM and for the identification of the ISL. Two indices of stationarity (IST) defined here are in essence similar to the steady-state test described by Foken & Wichura (1996):

$$IST_{wspd} = \frac{\left| \frac{1}{12} \sum_{i=1}^{12} \sigma_u^{i\,2} - \sigma_u^2 \right|}{\sigma_u^2}, \tag{3.1}$$

$$IST_{wdir}(°) = |wdir_{5min} - wdir_{1h}|_{max}. \tag{3.2}$$

In (3.1), $\sigma_u^{i\,2}$ is the streamwise velocity variance for each 5 min block within the 1 h run, and σ_u^2 is the variance for the entire hour. In (3.2), the notation $|\cdot|_{max}$ represents the maximum difference between the wind direction observed at a 5 min interval and the wind direction observed at a 1 h interval, among the 12 individual blocks. When the value of IST is small (close to zero), the streamwise velocity time series can be viewed as stationary. As the value of IST increases, the non-stationarity effects become significant. According to Moncrieff *et al.* (2004), $IST_{wspd} < 30\,\%$ should be achieved to ensure stationarity of the u time series, and this metric is employed here.

(iii) Presence of a constant σ_w. An index $I_{\sigma_w} = |\sigma_w - \langle \sigma_w \rangle|/\langle \sigma_w \rangle$ is defined to measure the deviation of the vertical velocity standard deviation at each level from its depth-averaged value ($\langle \sigma_w \rangle$) across the ISL. A small value suggests that the vertical velocity

standard deviation is vertically uniform consistent with the AEM. The necessary conditions for the vertical velocity variance to be invariant with z in the ISL may be derived from the mean vertical velocity equation for stationary, planar homogeneous flow in the absence of subsidence at very high Reynolds number. For these idealized conditions, the vertical velocity variance is given by

$$\frac{\partial \sigma_w^2}{\partial z} = -\left(\frac{1}{\rho}\right)\left(\frac{\partial \overline{P}}{\partial z}\right) - g, \tag{3.3}$$

where $\overline{P}$ is the mean pressure. When $\overline{P} = -\rho g z$ (i.e. hydrostatic), $\partial \sigma_w^2/\partial z = 0$ or σ_w^2 is constant with respect to z within the ISL. That is, the AEM requires $\overline{P}$ to be hydrostatic above and beyond the zero-pressure gradient condition needed to ensure a constant turbulent stress with z. The effects of adverse pressure gradients on C_1 have already been reported in wind tunnels and pipes (Turan *et al.* 1987). In the absence of mean pressure gradients, values of C_1 varying from 0.90 to 0.92 have been reported. Interestingly, for large adverse pressure gradients, a -1 power law was still reported, but values of C_1 as high as 17 were computed (Turan *et al.* 1987). These laboratory experiments underscore connections between the aforementioned constant σ_w^2 with z, finite mean pressure gradients, and the numerical values of C_1 and A_1.

(iv) Reynolds number. As earlier noted, sufficiently large Reynolds numbers are necessary when applying the AEM, allowing for self-similarity of turbulent structures (Townsend 1976). Numerous studies highlight the importance of high Reynolds numbers in validating the AEM and observing the expected turbulent behaviour (Marusic *et al.* 2010; Smits *et al.* 2011; Banerjee & Katul 2013; Huang & Katul 2022). Therefore, the dependency of fitted A_1 on Re_τ is also investigated. To calculate a bulk Reynolds number analogous to what is reported in laboratory studies, δ must be estimated. No direct measurement of δ is available during the experiment, and the boundary layer height is estimated from $\delta = C_a u_*/f_c$, where C_a is a dimensionless empirical constant typically varying between 0.07 and 0.3 (Seibert *et al.* 2000). Here, $C_a = 0.1$ is used after examining the streamwise energy spectrum as discussed later, and f_c is the Coriolis parameter given by $f_c = 2\Omega \sin(\phi)$, where Ω is the angular velocity of the Earth, and ϕ is the latitude of the location (Zilitinkevich 1972). While we acknowledge that the uncertainties of C_a can introduce uncertainties in the magnitude of the calculated boundary layer height δ and the bulk Reynolds number Re_τ, these uncertainties will not alter our main finding.

Before examining how fitted A_1 is affected by these individual factors mentioned above, it is noted that these factors are not entirely independent of each other. Figure 7(a) reveals a moderate negative correlation between R^2 and IST_{wspd}, indicating that increased non-stationarity in wind speed reduces the quality of the logarithmic fit. A weak negative correlation between R^2 and IST_{wdir} suggests a discernible decrease in fit quality with higher wind direction non-stationarity. More dynamically interesting is that higher computed Reynolds numbers (Re_τ) are positively correlated with a better fitting quality (R^2), agreeing with the basic assumption of the AEM. Non-stationarity in wind speed (IST_{wspd}) is negatively correlated with Re_τ, and greater deviations in the vertical velocity standard deviation (I_{σ_w}) and higher non-stationarity indices tend to occur at lower Reynolds numbers. Overall, a smaller Re_τ reflects, to some extent, the non-stationarity effect and the absence of a constant σ_w, all of which implicitly affect the fitting quality for the constants of the AEM at very high Re_τ. Therefore, the analysis focuses primarily on the role of Re_τ in describing the variations in fitted A_1 values.
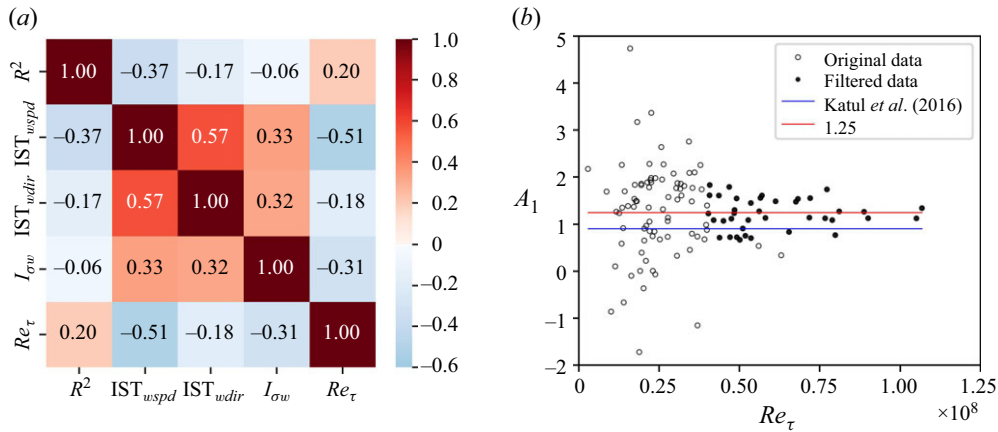
Figure 7. (*a*) Correlation heatmap between R^2 (coefficient of determination from the logarithmic fitting of the streamwise velocity variance), IST_{wspd} (non-stationarity index of wind speed), IST_{wdir} (non-stationarity index of wind direction), I_{σ_w} (absolute deviation of vertical velocity standard deviation from its mean across the ISL), and Re_τ (the bulk Reynolds number). Note that IST_{wspd}, IST_{wdir} and I_{σ_w} are calculated at every height and then averaged across the ISL. (*b*) Relation between A_1 and Re_τ. Open circles represent the original 120 neutral cases, while closed circles denote the 39 cases with $Re_\tau > 4 \times 10^7$ and $R^2 > 0.6$. The blue line represents the relation between A_1 and Re_τ as described in Katul *et al.* (2016), assuming $A_1 = C_1 = C_{o,u}\kappa^{-2/3}$, where $C_{o,u}$ is the Kolmogorov constant for the one-dimensional streamwise velocity spectrum in the inertial subrange (= 0.49). The red line denotes $A_1 = 1.25$.

Figure 7(*b*) illustrates that the derived A_1 values vary appreciably at lower Reynolds numbers but tend to converge asymptotically towards a relatively constant range around 1.25 as Re_τ increases. This suggests that despite the ASL Reynolds numbers being on the order of 10^7, the fitted A_1 values remain dependent on the Reynolds number. But here we should again highlight that the Reynolds number effect is correlated with other factors such as non-stationarity, thus this Reynolds number dependence of A_1 cannot be strictly interpreted as the dependence of A_1 on the scale separation in turbulent flows (Marusic *et al.* 2010; Smits *et al.* 2011; Banerjee & Katul 2013; Huang & Katul 2022).

When $Re_\tau > 4 \times 10^7$ is used as the criterion, 41 cases remain, all of which satisfy $\mathrm{IST}_{wspd} < 30\,\%$. To determine an appropriate threshold for R^2 values and identify potential outliers, the interquartile range (IQR) method (Komorowski *et al.* 2016) is applied. Outliers are defined as values outside the range ($Q_1 - 1.5 \times IQR$, $Q_3 + 1.5 \times IQR$), where Q_1, Q_3 are defined as the 25th and 75th percentiles of the data, and $IQR = Q_3 - Q_1$. For the 41 cases, the IQR analysis of R^2 values results in $Q_1 - 1.5 \times IQR = 0.62$. Based on this analysis, $R^2 > 0.6$ has been adopted as the threshold for excluding outliers. This removes two outliers, shown as open circles. Therefore, the subsequent analysis focuses on the 39 cases where $R^2 > 0.6$ and $Re_\tau > 4 \times 10^7$.

Table 3 and 4 present the results before and after applying the criteria $Re_\tau > 4 \times 10^7$ and $R^2 > 0.6$. After these quality controls are applied, the mean value of A_1 changes from 1.25 to 1.22. The mean value of κ remains consistent (from 0.37 to 0.38), though with a reduced standard deviation. The R^2 values show marked improvement, and the non-stationarity indices decrease substantially. The vertical variability of σ_w also decreases from 0.03 to 0.02.

Post-screening, the patterns of near-neutral occurrence hours and wind directions remain consistent with the previous data. Instances that are infrequent pre-screening become even rarer after the screening, while common instances become more frequent (see figure 3*c*,*d*). The double rotation and planar fit methods show even smaller differences

Variable	Mean	Std	Mean	Std
R^2	0.81	0.23	0.88	0.08
IST_{wspd}	0.13	0.11	0.07	0.04
IST_{wdir}	8.03	5.74	7.21	3.48
I_{σ_w}	0.03	0.02	0.02	0.01
Re_τ	3.66×10^7	2.12×10^7	6.06×10^7	1.76×10^7

Table 4. Comparison of mean and standard deviation (Std) before and after applying the screening $Re_\tau > 4 \times 10^7$ and $R^2 > 0.6$. Variables are defined as in figure 7.

(see table 3). The analysis indicates that the variations in A_1 are driven primarily by non-stationarity considerations and Reynolds number dependence. However, the variability of A_1 (standard deviation 0.33) remains non-trivial compared to the classical values derived from laboratory experiments, despite all the data quality controls imposed on these ASL measurements. This highlights the complexity of ASL flows, necessitating case-by-case investigations, which will be discussed in § 3.3.2.

3.2.3. *Effect of stability*

In unstable conditions, thermal plumes enhance vertical mixing and modify the turbulent eddy structure. In stable conditions, near-surface turbulence and the residual layer above it progressively decouple with increasing stability, reducing the influence of ABL-scale motions on near-surface turbulence, and diminishing the size of streamwise streaks. In those conditions, near-surface turbulence becomes intermittent (Dupont & Patton 2022). These modifications can influence the streamwise velocity variance and energy spectra, including the k^{-1} scaling (Banerjee *et al.* 2015). In our study, $|z_{mean}/L_{median}| < 0.1$ is used to select near-neutral cases, which is not a strict condition. Whether the selected cases are still influenced by some remaining buoyancy effects (especially the higher z measurements) is now considered.

It is observed that sensible heat flux magnitude ($|H|$) shows a strong positive correlation with Re_τ (correlation coefficient 0.65), indicating that higher sensible heat fluxes tend to be associated with higher Reynolds numbers. Given a constant C_a used in this study, the correlation between sensible heat flux magnitude and Re_τ is caused by the friction velocity (u_*). At our site, higher friction velocities are generally associated with higher sensible heat fluxes, maintaining near-neutral stability in the ASL.

Figure 8(a) illustrates the relation between the stability parameter and the fitted A_1. The screening criteria $Re_\tau > 4 \times 10^7$ and $R^2 > 0.6$ exclude data with stability parameters greater than 0.026 (positive, stable) and less than -0.05 (negative, unstable). The remaining data are approximately evenly distributed across the range $(-0.05, 0.025)$ with no significant trend. This suggests that there is little stability effect on A_1 after screening. This finding is not sensitive to the criterion $|z_{mean}/L_{median}| < 0.1$, which justifies its initial choice for indicating near-neutral conditions.

In contrast, the influence of stability conditions on the fitted values of κ is visible in figure 8(b). Even after applying the stability constraint, the fitted κ values remain influenced by variations in atmospheric stability. This finding is consistent with Andreas *et al.* (2006), who reported a range of κ values between 0.2 and 0.6 for $-0.1 < z/L < 0.1$ in their figure 6. It is possible to correct the stability effect on κ by employing MOST and the Businger–Dyer relation for the stability correction function (Businger 1988). After correcting the stability effects, the median value of κ estimated from the dataset analysed
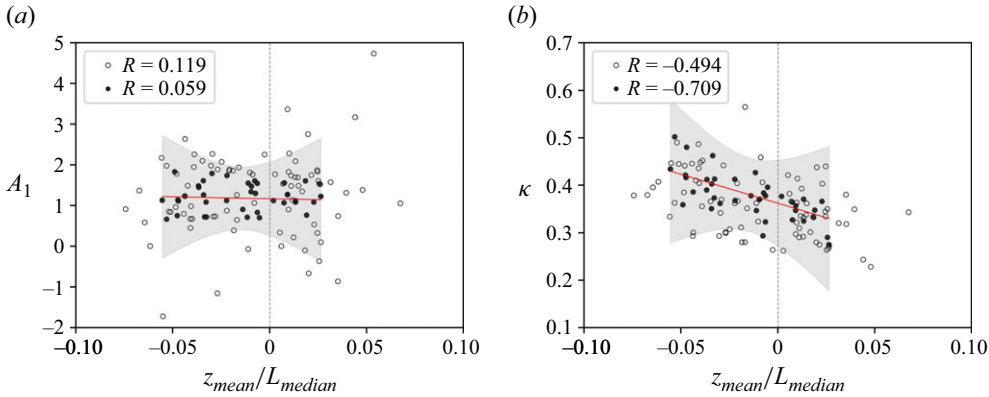
Figure 8. Relations between (*a*) the fitted A_1 and (*b*) the fitted κ and stability parameters z_{mean}/L_{median}. Vertical dashed lines represent $z_{mean}/L_{median} = 0$, solid red lines denote the linear regression of the data, grey shadings denote the 95th confidence level, and closed circles denote the 39 cases with $Re_\tau > 4 \times 10^7$ and $R^2 > 0.6$. Note that two outliers in (*a*) and 3 outliers in (*b*) are not shown, for better visualization. The legends give the correlation coefficients (*R*).

here is 0.36. This aligns with figure 8(*b*), where the vertical dashed line intersects the regression line approximately at $\kappa = 0.36$.

3.3. *Streamwise velocity energy spectrum*

3.3.1. *Ensemble streamwise velocity energy spectrum*

The pre-multiplied streamwise velocity energy spectra are computed within the ISL using the Welch method (Welch 1967) while applying a Hann window with a 2^{14} window size and 50% overlap between consecutive windows. The power spectral density is then interpolated onto 500 logarithmically spaced frequencies, spanning from 10^{-4} Hz to 5 Hz (Nyquist frequency). Figure 9 shows the ensemble average (i.e. average over 39 post-screening cases) of the pre-multiplied *u*-spectra. The streamwise wavenumber *k* is calculated based on Taylor's hypothesis as $k = 2\pi f/\overline{u}$, where *f* is the frequency. Due to the normalization of wavenumbers by *z* (figure 9*b*), the pre-multiplied spectra at different heights collapse well in the inertial subrange (Kaimal & Finnigan 1994). The pre-multiplied *u*-spectrum rises at the tail due to high-frequency noise. However, this high-frequency noise does not significantly affect the streamwise velocity variance, and is neglected.

A $k^{-2/3}$ power-law scaling is evident in the inertial subrange wavenumber region, consistent with Kolmogrov's theory. More interestingly, a plateau of approximately 1–1.25 begins at $k\delta \approx 1$ (see figure 9*a*), consistent with the onset of the k^{-1} scaling predicted by the AEM, suggesting that the estimation of $\delta = C_a u_*/f_c$ with $C_a = 0.1$ is plausible. Furthermore, this plateau occurs within the range $\mathcal{O}(0.1) < kz < \mathcal{O}(1)$, as shown in figure 9(*b*), indicating a robust k^{-1} power-law scaling for $E_{uu}(k)$. However, the k^{-1} scaling region is just under a decade in extent, prompting the question of whether individual cases show clear k^{-1} scaling and whether the plateau values (C_1) correspond to the fitted A_1 values, which will be discussed next.

3.3.2. *Additional quality control*

To analyse the linkage between the logarithmic behaviour of streamwise velocity variance and the k^{-1} scaling in the streamwise energy spectra (E_{uu}), each of the 39 remaining cases is examined individually; C_1 is approximated by the 95th percentile values of $k E_{uu}/u_*^2$ for
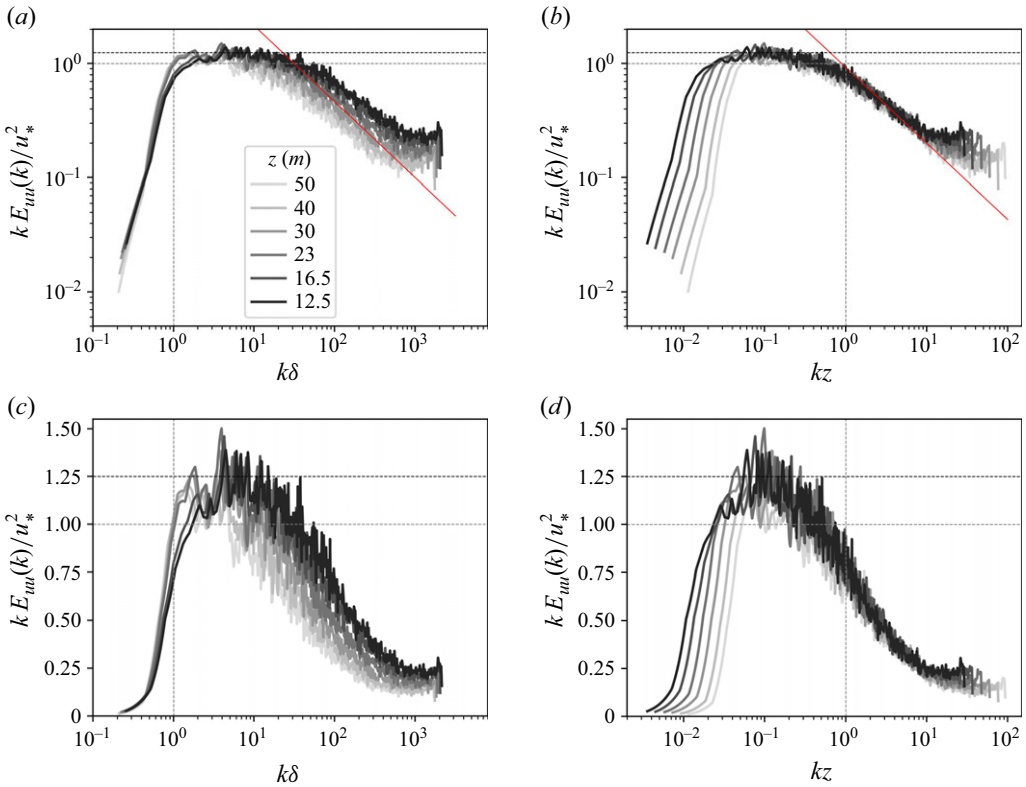
Figure 9. The ensemble average of the pre-multiplied streamwise velocity spectrum over 39 post-screening cases, from 12.5 m (lightest shade) to 50 m (darkest shade), with (*a*) δ scaling and (*b*) z scaling. Horizontal dashed lines mark 1 and 1.25. Vertical dashed lines indicate that $k\delta$ or kz equals 1. Solid red lines denote the $-2/3$ scaling. (*c,d*) The same as (*a*) and (*b*), respectively, but using a linear vertical axis scale.

simplicity. Although this is an approximation, it enables us to explore a general correlation between A_1 and C_1.

The profile of the vertical velocity variance and the TKE budget are also examined. In the ISL, the TKE budget simplifies to a balance between the mechanical production (P) and the viscous dissipation rate (ϵ). The production rate is determined by

$$P = u_*^2 \frac{\partial U}{\partial z},\tag{3.4}$$

where $\partial U/\partial z$ is approximated in two ways: first, using $u_*/\kappa z$ based on the log law, where κ is the fitted value; second, using a third-order polynomial fitting with respect to $\ln(z)$ applied to the mean wind profile across all 12 levels. These two methods yield similar results (as shown in figure 12*a* in Appendix A). The production rate obtained using the second method is used in the analysis of the TKE budget. The dissipation rate (ϵ) is determined by both the second-order structure functions ($D_2(r)$) and the third-order structure functions ($D_3(r)$), respectively. At very high Reynolds numbers, these are given as

$$D_2(r) = C_2 \epsilon^{2/3} r^{2/3},\tag{3.5a}$$

$$D_3(r) = -\frac{4}{5}\epsilon r, \tag{3.5b}$$

where C_2 is a coefficient (≈ 1.97 for one-dimensional wavenumber), and r represents the separation distance in the streamwise direction, set to be the minimum between 1 m and $z/2$ (Chamecki & Dias 2004). Prior studies have shown that the ratio of $D_2(r)$ in the vertical to the streamwise direction most closely matches the isotropic value $4/3$ when $0.63 \leqslant r \leqslant 1.0$ (Chamecki & Dias 2004). A similar eddy size range was also identified in other ASL experiments (Katul *et al.* 1997). Figure 12b shows that the dissipation rates derived from the third-order structure function are slightly smaller than their second-order counterparts. The Taylor hypothesis is invoked here to compute $D_2(r)$ and $D_3(r)$. In the following analysis, both dissipation rates are used to assess the sensitivity of the AEM to TKE dissipation rate estimation.

The 39 cases analysed are categorized into five distinct groups based on their turbulent properties.

(i) Group 1. This group includes three cases with anomalous σ_u^2 profiles (figure 13), characterized by deviations in the streamwise velocity variance that do not align with the logarithmic shape.

(ii) Group 2. Nine cases are categorized as exhibiting anomalous σ_w^2 profiles, with distinct trends evident within the ISL (figure 14).

(iii) Group 3. Seven cases are classified as having anomalous E_{uu} profiles, where the pre-multiplied streamwise velocity spectrum displays two or more peaks in the production range (figure 15). This might be related to the influence of very-large-scale detached eddies.

(iv) Group 4. Five cases exhibit an anomalous TKE balance (figure 16), where the ratio of production to dissipation rates shows discernible trends in the ISL. These trends likely indicate non-equilibrium turbulence, potentially driven by sudden changes in wind speed, temperature gradients, or other transient meteorological phenomena.

(v) Group 5. Nine cases are identified as high-quality data, serving as benchmarks for analysis. These cases exhibit canonical turbulent behaviour and are used to investigate the connection between streamwise velocity variance and the streamwise velocity energy spectrum.

Anomalous behaviours identified in groups 1–4 may overlap, but such overlaps are not addressed explicitly in this categorization. It is emphasized that all cases – both anomalous and benchmark – passed the objective data quality control procedures outlined in § 3.2.2. The anomalies observed in groups 1–4 may stem from local topographic influences, instrumentation issues, or transient meteorological phenomena.

Figure 10 provides an example of the high-performance group 5, on 29 March 2021, at 04:00 LT. The profile of σ_u^2 exhibits a logarithmic behaviour, with a fitted $A_1 = 1.12$ (figure 10a). Similar to the ensemble average, the pre-multiplied E_{uu} reach a plateau in the range $\mathcal{O}(0.02) < kz < \mathcal{O}(1)$. The estimated C_1 is 1.23, marginally higher than the fitted A_1. At the inertial subrange, the streamwise energy spectra align well with a $k^{-2/3}$ scaling (figure 10b), as expected. The vertical velocity variance remains constant with z in the ISL (figure 10c), with the σ_w^2/u_*^2 values centred around 1.3. The ratio P/ϵ derived from both $D_2(r)$ and $D_3(r)$ is invariant with height within the ISL. However, P/ϵ based on $D_2(r)$ is smaller than that based on $D_3(r)$, with the latter being close to unity.
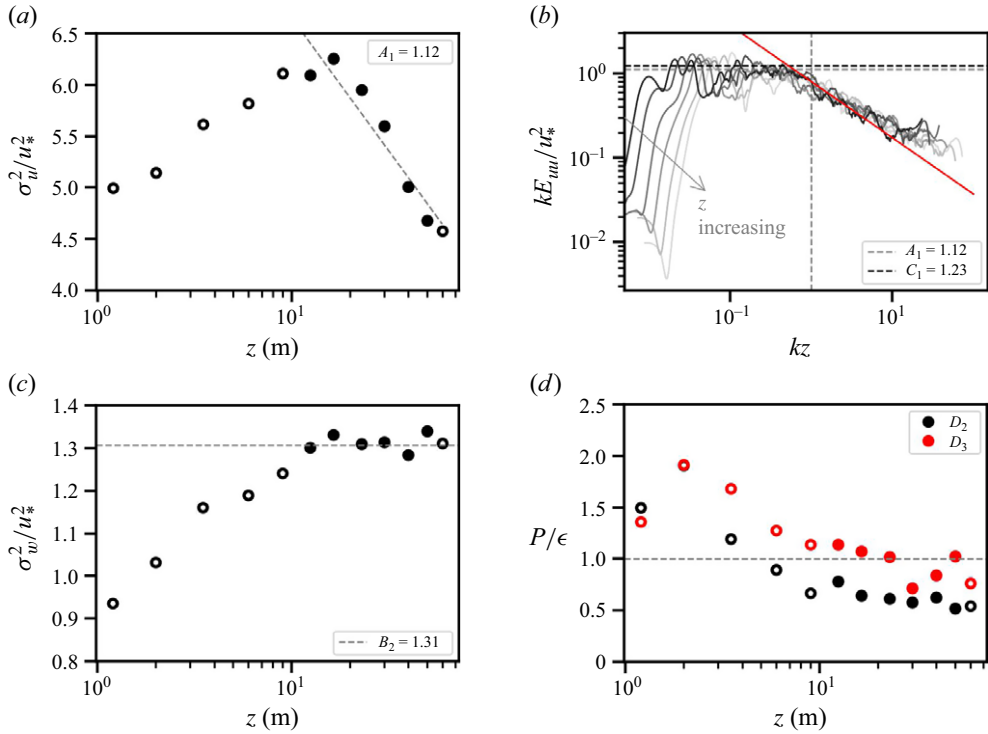
Figure 10. An example of a benchmark case collected on 29 March 2021, at 04:00 LT. (*a*) Profile of σ_u^2. The dashed grey line denotes the linear regression of the data within the ISL, indicating the fitted $A_1 = 1.12$ of this case. (*b*) The pre-multiplied streamwise velocity spectrum normalized by u_* (kE_{uu}/u_*^2) against wavenumber normalized by height (kz). The arrow represents increasing z. The vertical dashed line marks $kz = 1$. Horizontal dashed lines mark the fitted $A_1 = 1.12$ (in grey) and $C_1 = 1.23$ (in black) estimated by the depth-average of the 95th percentile of kE_{uu}/u_*^2. The solid red line denotes the $-2/3$ scaling. (*c*) Profile of σ_w^2. The dashed grey line represents the estimated $B_2 = 1.31$. (*d*) The ratio of production rate p to dissipation rate ϵ against z. Here, p is calculated by the third-order polynomial fitting of the mean wind profile, and ϵ is calculated using both the second-order structure function (in black) and the third-order structure function (in red). The dashed grey line represents where $P/\epsilon = 1$. Closed circles indicate the selected ISL.

To investigate whether a $C_1 = A_1$ relation can be observed in the adiabatic ASL, the estimated A_1 and C_1 of the 39 post-filtered cases are grouped based on these additional quality controls, and plotted against Re_τ (see figure 11*a*). Each vertical line connects the open and closed symbols for the same Re_τ, indicating the difference between the corresponding A_1 and C_1 for each case within the groups. In groups 1, 3 and 4, the estimated C_1 values differ strongly from their corresponding A_1 values. Groups 2 and 5 exhibit a spread of A_1 and C_1 values across different Re_τ. Interestingly, while there are strong differences between A_1 and C_1 at lower Re_τ, they appear to converge at higher Re_τ for groups 2 and 5. However, the limited data points prevent a more definitive conclusion. Figure 11(*b*) further explores the correspondence between A_1 and C_1, which seems to be better for groups 5 and 2 than groups 1, 3 and 4, consistent with the results in figure 11(*a*). Nonetheless, the limited data points, the narrow range of values used for the comparison, and the associated weak correlations between A_1 and C_1 do not provide concrete support for the $C_1 = A_1$ relation.
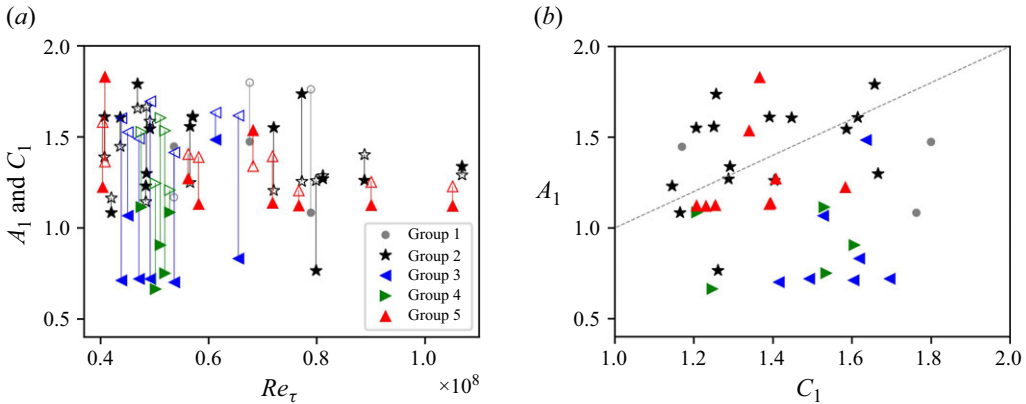
Figure 11. (*a*) Relation between the fitted A_1 (closed symbols) as well as the estimated C_1 (open symbols) against Re_τ. Group 1: 3 cases with anomalous σ_u^2 profiles denoted by grey circles. Group 2: 9 cases with anomalous σ_w^2 profiles denoted by black stars. Group 3: 7 cases with anomalous E_{uu} profiles denoted by blue left-pointing triangles. Group 4: 5 cases with anomalous TKE budget balance denoted by green right-pointing triangles. Group 5: 9 cases with high performance denoted by red upward triangles. (b) Relation between the estimated C_1 and the fitted A_1. The grey dashed line denotes the one-to-one line.

4. Conclusions

The logarithmic behaviour of the streamwise velocity variance (σ_u^2) in the near-neutral ASL predicted by the AEM is explored using eddy-covariance measurements from a 62 m tower located in the Eastern Snake River Plain, Idaho, USA. Additionally, the study examines the relation between the AEM similarity coefficient associated with the z scaling of σ_u^2, and the similarity coefficient describing $u_*^2 k^{-1}$ in the streamwise energy spectra at production scales.

The analysis indicates that the streamwise velocity variance in the near-neutral ASL follows a logarithmic profile within the inertial sublayer (ISL). The fitted value of the Townsend–Perry coefficient (A_1) associated with the AEM is sensitive to weak non-stationarity. To bypass this issue, high-pass filtering is needed to remove any nonlinear trends. In contrast, the fitted von Kármán constant (κ) to the mean velocity profile is not as sensitive to these effects, but is influenced by mild deviations in the atmospheric stability conditions from neutral conditions.

The variability in the fitted value of A_1 is largely attributed to non-stationarity, Reynolds number dependence, and quality of the fitting process, factors that are interrelated rather than completely independent. After controlling for these factors, 39 hours of data remain, and their fitted A_1 values converge to the range 1.0–1.25. However, this variability is non-trivial (mean 1.22, standard deviation 0.33, minimum 0.67, maximum 1.83).

A further selection of nine cases with canonical σ_u^2 and σ_w^2 profiles, E_{uu} shapes, and expected TKE budget balance between production and dissipation reveals that, in these cases, the pre-multiplied E_{uu} reaches a plateau in the production range, spanning approximately a decade, equivalent to a k^{-1} scaling in E_{uu}. Both the fitted A_1 and the estimated C_1 display some scatter at lower Re_τ, but as Re_τ increases, relatively tighter and more consistent values between A_1 and C_1 emerge (i.e. $A_1 = C_1$). Further investigations with more data are needed to confirm (or refute) the equivalence between A_1 and C_1.

These findings suggest that near-neutral ASL turbulence does obey the AEM, with coefficients commensurate with those reported for very high Reynolds number laboratory experiments. It also highlights the complexity of the ASL, where non-stationary effects,

large-scale and very-large-scale eddies, and local topographic features complicate the identification of the ISL in streamwise velocity variance profiles and the k^{-1} scaling range in the streamwise energy spectrum. Future studies will explore two inter-related aspects of ISL flow statistics: the m higher-order moments of $(\sigma_u/u_*)^m$ for near neutral conditions, and the role of atmospheric stability in shaping the scaling laws of σ_u and its spectral behaviours at large scales.

Appendix A. Supplementary figures

Figure 12. (*a*) Comparison between the mechanical production rate calculated using the log law (P_{log}) and the polynomial fitting to mean velocity data (P_{poly}). (*b*) Comparison between the TKE dissipation rate calculated using the second-order structure function (ϵ_2) and the third-order structure function (ϵ_3). Grey dashed lines represent perfect agreement.
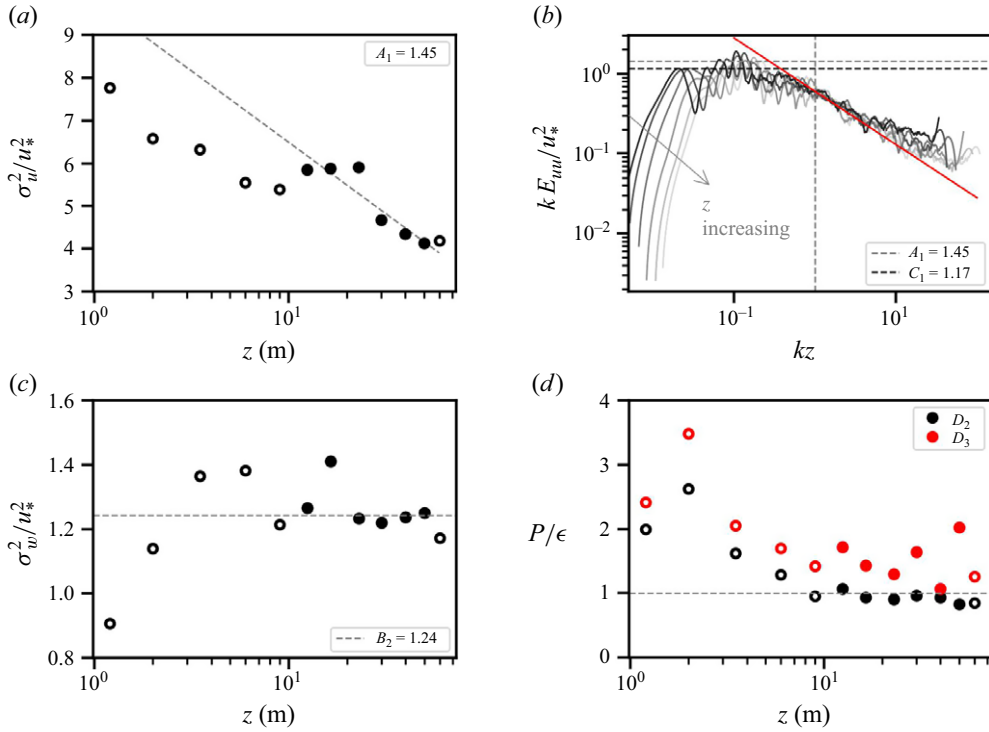
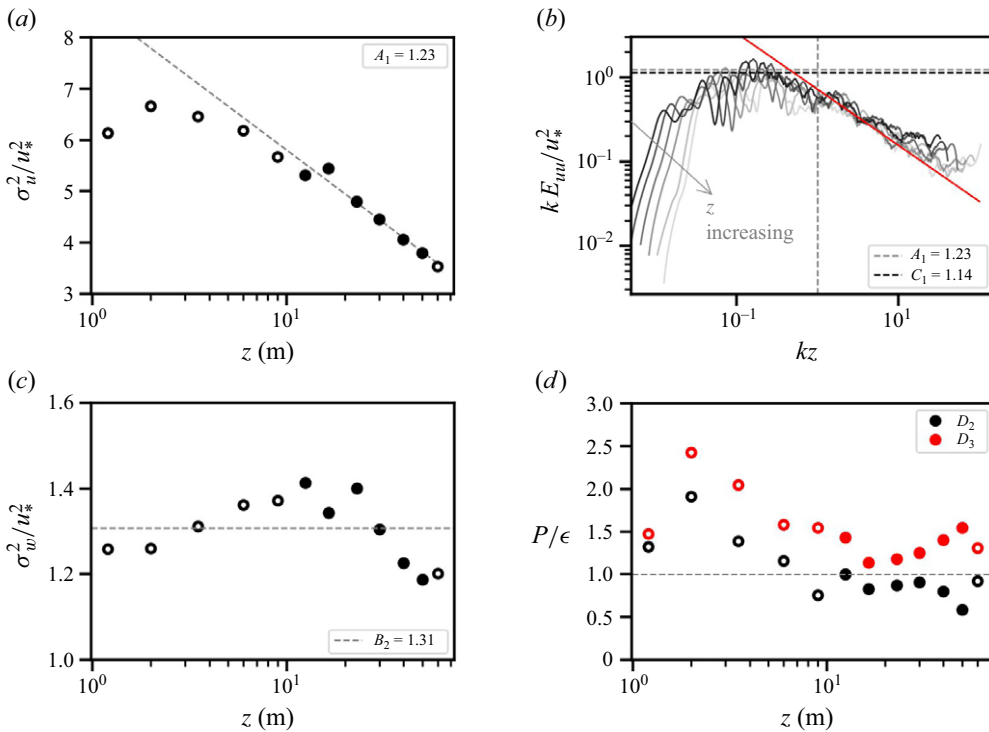Figure 13. Example of anomalous σ_u^2; similar to figure 10, with data from 6 March 2021, at 15:00 LT.

Figure 14. Example of anomalous σ_w^2; similar to figure 10, with data from 14 April 2021, at 11:00 LT.
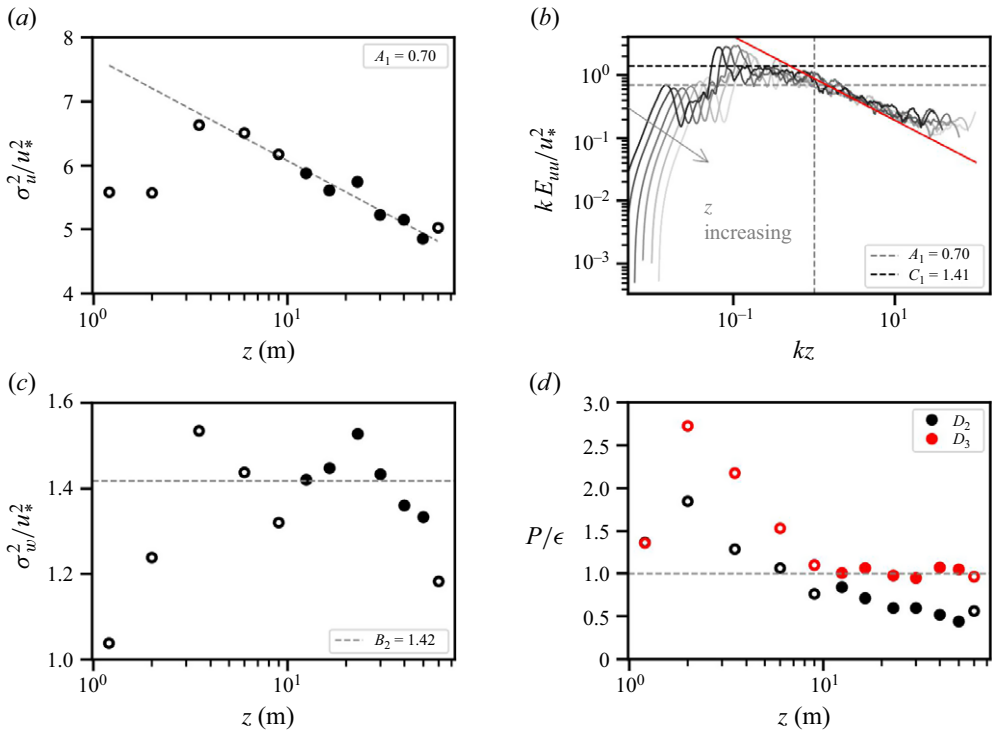
Figure 15. Example of anomalous E_{uu}; similar to figure 10, with data from 10 October 2020, at 16:00 LT.

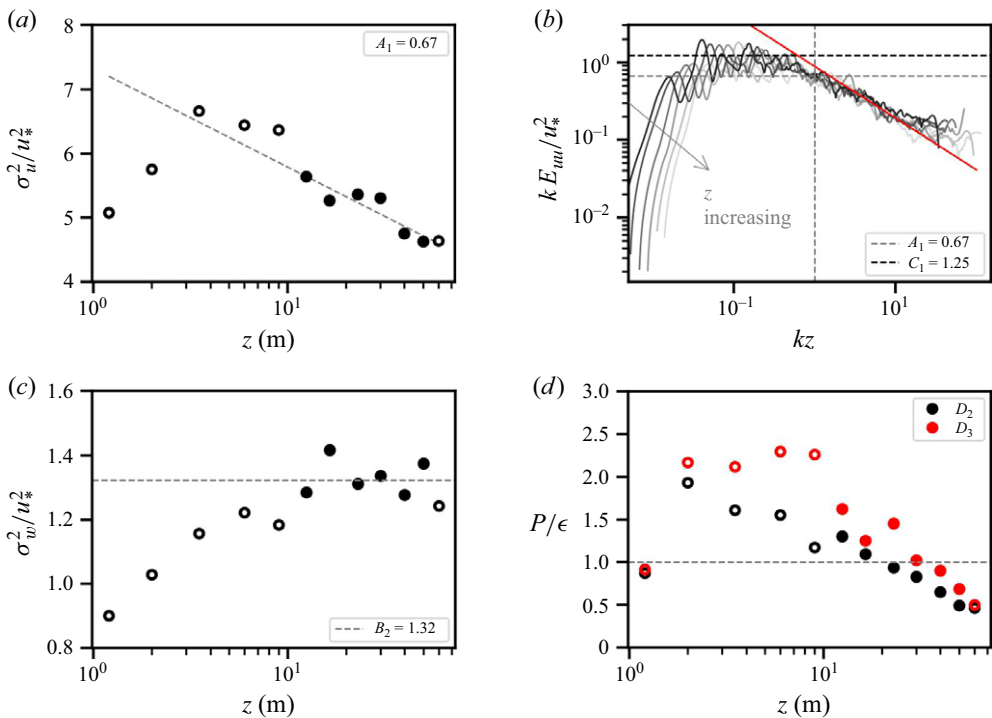
Figure 16. Example of anomalous TKE budget balance; similar to figure 10, with data from 19 November 2020, at 14:00 LT.

REFERENCES

ANDREAS, E.L., CLAFFY, K.J., JORDAN, R.E., FAIRALL, C.W., GUEST, P.S., PERSSON, P.O.G. & GRACHEV, A.A. 2006 Evaluations of the von Kármán constant in the atmospheric surface layer. *J. Fluid Mech.* **559**, 117–149.

ANTONIA, R.A. & RAUPACH, M.R. 1993 Spectral scaling in a high Reynolds number laboratory boundary layer. *Boundary-Layer Meteorol.* **65** (3), 289–306.

AUBINET, M., VESALA, T. & PAPALE, D. 2012 *Eddy Covariance: A Practical Guide to Measurement and Data Analysis*. Springer Science & Business Media.

BAARS, W.J. & MARUSIC, I. 2020 Data-driven decomposition of the streamwise turbulence kinetic energy in boundary layers. Part 1. Energy spectra. *J. Fluid Mech.* **882**, A25.

BANERJEE, T. & KATUL, G.G. 2013 Logarithmic scaling in the longitudinal velocity variance explained by a spectral budget. *Phys. Fluids* **25** (12), 125106.

BANERJEE, T., KATUL, G.G., SALESKY, S.T. & CHAMECKI, M. 2015 Revisiting the formulations for the longitudinal velocity variance in the unstable atmospheric surface layer. *Q. J. R. Meteorol. Soc.* **141** (690), 1699–1711.

BANTA, R.M., PICHUGINA, Y.L. & BREWER, W.A. 2006 Turbulent velocity-variance profiles in the stable boundary layer generated by a nocturnal low-level jet. *J. Atmos. Sci.* **63** (11), 2700–2719.

BRADSHAW, P. 1967 'Inactive' motion and pressure fluctuations in turbulent boundary layers. *J. Fluid Mech.* **30** (2), 241–258.

BRADSHAW, P. 1978 Comments on 'Horizontal velocity spectra in an unstable surface layer'. *J. Atmos. Sci.* **35** (9), 1768–1769.

BREMHORST, K. & BULLOCK, K.J. 1970 Spectral measurements of temperature and longitudinal velocity fluctuations in fully developed pipe flow. *Intl J. Heat Mass Transfer* **13** (8), 1313–1329.

BULLOCK, K.J., COOPER, R.E. & ABERNATHY, F.H. 1978 Structural similarity in radial correlations and spectra of longitudinal velocity fluctuations in pipe flow. *J. Fluid Mech.* **88** (3), 585–608.

BUSINGER, J.A. 1988 A note on the Businger–Dyer profiles. In *Topics in Micrometeorology. A Festschrift for Arch Dyer* (ed. B.B. Hicks), pp. 145–151. Springer.

CHAMECKI, M. & DIAS, N.L. 2004 The local isotropy hypothesis and the turbulent kinetic energy dissipation rate in the atmospheric surface layer. *Q. J. R. Meteorol. Soc.* **130** (603), 2733–2752.

CLAUSER, F.H. 1956 The turbulent boundary layer. *Adv. Appl. Mech.* **4**, 1–51.

CLAWSON, K.L., RICH, J.D., ECKMAN, R.M., HUKARI, N.F., FINN, D. & REESE, B.R. 2018 Climatography of the Idaho National Laboratory, 4th edition. *NOAA Technical Memorandum OAR* ARL-278. NOAA Air Resources Laboratory.

DUPONT, S. & PATTON, E.G. 2022 On the influence of large-scale atmospheric motions on near-surface turbulence: comparison between flows over low-roughness and tall vegetation canopies. *Boundary-Layer Meteorol.* **184** (2), 195–230.

ERM, L.P. & JOUBERT, P.N. 1991 Low-Reynolds-number turbulent boundary layers. *J. Fluid Mech.* **230**, 1–44.

FARR, T.G. *et al.* 2007 The shuttle radar topography mission. *Rev. Geophys.* **45** (2), RG2004.

FINN, D., CLAWSON, K.L., ECKMAN, R.M., LIU, H., RUSSELL, E.S., GAO, Z. & BROOKS, S. 2016 Project Sagebrush: revisiting the value of the horizontal plume spread parameter σ_y. *J. Appl. Meteorol. Climatol.* **55**, 1305–1322.

FINN, D., CARTER, R.G., ECKMAN, R.M., RICH, J.D., GAO, Z. & LIU, H. 2018a Plume dispersion in low-wind-speed conditions during Project Sagebrush Phase 2, with emphasis on concentration variability. *Boundary-Layer Meteorol.* **169** (1), 67–91.

FINN, D., ECKMAN, R.M., GAO, Z. & LIU, H. 2018b Mechanisms for wind direction changes in the very stable boundary layer. *J. Appl. Meteorol. Climatol.* **57** (11), 2623–2637.

FOKEN, T. & WICHURA, B. 1996 Tools for quality assessment of surface-based flux measurements. *Agric. Forest Meteorol.* **78** (1–2), 83–105.

GAO, Z., LIU, H., LI, D., YANG, B., WALDEN, V., LI, L. & BOGOEV, I. 2024 Uncertainties in temperature statistics and fluxes determined by sonic anemometers due to wind-induced vibrations of mounting arms. *Atmos. Meas. Tech.* **17** (13), 4109–4120.

GARRETT, J.R. 1994 *The Atmospheric Boundary Layer*. Cambridge University Press.

HÖGSTRÖM, U., HUNT, J.C.R. & SMEDMAN, A.-S. 2002 Theory and measurements for turbulence spectra and variances in the atmospheric neutral surface layer. *Boundary-Layer Meteorol.* **103** (1), 101–124.

HUANG, K.Y. & KATUL, G.G. 2022 Profiles of high-order moments of longitudinal velocity explained by the random sweeping decorrelation hypothesis. *Phys. Rev. Fluids* **7** (4), 044603.

HULTMARK, M., VALLIKIVI, M., BAILEY, S.C.C. & SMITS, A.J. 2012 Turbulent pipe flow at extreme Reynolds numbers. *Phys. Rev. Lett.* **108** (9), 094501.

HUTCHINS, N., CHAUHAN, K., MARUSIC, I., MONTY, J. & KLEWICKI, J. 2012 Towards reconciling the large-scale structure of turbulent boundary layers in the atmosphere and laboratory. *Boundary-Layer Meteorol.* **145** (2), 273–306.

HWANG, Y., HUTCHINS, N. & MARUSIC, I. 2022 The logarithmic variance of streamwise velocity and conundrum in wall turbulence. *J. Fluid Mech.* **933**, A8.

KADER, B.A. & YAGLOM, A.M. 1991 Spectra and correlation functions of surface layer atmospheric turbulence in unstable thermal stratification. In *Turbulence and Coherent Structures* (ed. J.C.R. HUNT, O.M. PHILLIPS & D. WILLIAMS), pp. 387–412. Springer.

KAIMAL, J.C. 1978 Horizontal velocity spectra in an unstable surface layer. *J. Atmos. Sci.* **35** (1), 18–24.

KAIMAL, J.C. & FINNIGAN, J.J. 1994 *Atmospheric Boundary Layer Flows: Their Structure and Measurement*. Oxford University Press.

KATUL, G. & CHU, C.R. 1998 A theoretical and experimental investigation of energy-containing scales in the dynamic sublayer of boundary-layer flows. *Boundary-Layer Meteorol.* **86** (2), 279–312.

KATUL, G., HSIEH, C.I. & SIGMON, J. 1997 Energy-inertial scale interactions for velocity and temperature in the unstable atmospheric surface layer. *Boundary-Layer Meteorol.* **82** (1), 49–80.

KATUL, G.G., BANERJEE, T., CAVA, D., GERMANO, M. & PORPORATO, A. 2016 Generalized logarithmic scaling for high-order moments of the longitudinal velocity component explained by the random sweeping decorrelation hypothesis. *Phys. Fluids* **28** (9), 095104.

KATUL, G.G., CHU, C.R., PARLANGE, M.B., ALBERTSON, J.D. & ORTENBURGER, T.A. 1995 Low-wavenumber spectral characteristics of velocity and temperature in the atmospheric surface layer. *J. Geophys. Res.* **100** (D7), 14243–14255.

KATUL, G.G., PORPORATO, A., MANES, C. & MENEVEAU, C. 2013 Co-spectrum and mean velocity in turbulent boundary layers. *Phys. Fluids* **25** (9), 091702.

KENDALL, A. & KOOCHESFAHANI, M. 2008 A method for estimating wall friction in turbulent wall-bounded flows. *Exp. Fluids* **44** (5), 773–780.

KLEBANOFF, P.S. 1954 *Characteristics of Turbulence in a Boundary Layer with Zero Pressure Gradient*. vol. 3178. National Advisory Committee for Aeronautics.

KOMOROWSKI, M., MARSHALL, D.C., SALCICCIOLI, J.D. & CRUTAIN, Y. 2016 Exploratory data analysis. In *Secondary Analysis of Electronic Health Records* (ed. MIT Critical Data). Springer International Publishing.

KULANDAIVELU, V. & MARUSIC, I. 2010 Evolution of zero pressure gradient turbulent boundary layers. In *Proceedings of the 17th Australasian Fluid Mechanics Conference*, pp. 196–201. Australasian Fluid Mechanics Society.

KUNKEL, G.J. & MARUSIC, I. 2006 Study of the near-wall-turbulent region of the high-Reynolds-number boundary layer using an atmospheric flow. *J. Fluid Mech.* **548**, 375–402.

LENSCHOW, D.H., MANN, J. & KRISTENSEN, L. 1994 How long is long enough when measuring fluxes and other turbulence statistics? *J. Atmos. Ocean. Technol.* **11** (3), 661–673.

LI, D. & BOU-ZEID, E. 2011 Coherent structures and the dissimilarity of turbulent transport of momentum and scalars in the unstable atmospheric surface layer. *Boundary-Layer Meteorol.* **140** (2), 243–262.

LUMLEY, J.L. & PANOFSKY, H.A. 1964 *The Structure of Atmospheric Turbulence*. Interscience Publishers (Wiley & Sons).

MARUSIC, I. & KUNKEL, G.J. 2003 Streamwise turbulence intensity formulation for flat-plate boundary layers. *Phys. Fluids* **15** (8), 2461–2464.

MARUSIC, I., MCKEON, B.J., MONKEWITZ, P.A., NAGIB, H.M., SMITS, A.J. & SREENIVASAN, K.R. 2010 Wall-bounded turbulent flows at high Reynolds numbers: Recent advances and key issues. *Phys. Fluids* **22** (6), 1–24.

MARUSIC, I. & MONTY, J.P. 2019 Attached eddy model of wall turbulence. *Annu. Rev. Fluid Mech.* **51** (1), 49–74.

MARUSIC, I., MONTY, J.P., HULTMARK, M. & SMITS, A.J. 2013 On the logarithmic region in wall turbulence. *J. Fluid Mech.* **716**, R3-1–R3-11

MARUSIC, I., UDDIN, A.K.M. & PERRY, A.E. 1997 Similarity law for the streamwise turbulence intensity in zero-pressure-gradient turbulent boundary layers. *Phys. Fluids* **9** (12), 3718–3726.

METZGER, M., MCKEON, B.J. & HOLMES, H. 2007 The near-neutral atmospheric surface layer: turbulence and non-stationarity. *Phil. Trans. R. Soc. Lond. A: Math. Phys. Engng Sci.* **365** (1852), 859–876.

MONCRIEFF, J., CLEMENT, R., FINNIGAN, J. & MEYERS, T. 2004 Averaging, detrending, and filtering of eddy covariance time series. In *Handbook of Micrometeorology: A Guide for Surface Flux Measurement and Analysis* (ed. X. Lee, W. Massman & B. Law), pp. 7–31. Springer.

MONIN, A.S. & YAGLOM, A.M. 1971 *Statistical Fluid Mechanics: Mechanics of Turbulence*, vol. 1. The MIT Press Series in Environmental Engineering Science. MIT Press.

MONIN, A.S. & OBUKHOV, A.M. 1954 Basic laws of turbulent mixing in the atmosphere near the ground. *Tr. Geofiz. Inst., Akad. Nauk SSSR* **24** (151), 163–187.

MORRISON, J.F., MCKEON, B.J., JIANG, W. & SMITS, A.J. 2004 Scaling of the streamwise velocity component in turbulent pipe flow. *J. Fluid Mech.* **508**, 99–131.

NAGIB, H.M. & CHAUHAN, K.A. 2008 Variations of von Kármán coefficient in canonical flows. *Phys. Fluids* **20**, 105105.

NICKELS, T.B., MARUSIC, I., HAFEZ, S. & CHONG, M.S. 2005 Evidence of the k_1^{-1} law in a high-Reynolds-number turbulent boundary layer. *Phys. Rev. Lett.* **95**, 074501.

NICKELS, T.B., MARUSIC, I., HAFEZ, S., HUTCHINS, N. & CHONG, M.S. 2007 Some predictions of the attached eddy model for a high Reynolds number boundary layer. *Phil. Trans. R. Soc. Lond. A: Math. Phys. Engng Sci.* **365** (1852), 807–822.

NIKORA, V. 1999 Origin of the '−1' spectral law in wall-bounded turbulence. *Phys. Rev. Lett.* **83** (4), 734–736.

OBUKHOV, A.M. 1946 Turbulentnost' v temperaturnoj-neodnorodnoj atmosfere. *Trudy Inst. Theor. Geofiz. AN SSSR* **1**, 95–115.

ÖSTERLUND, J.M., JOHANSSON, A.V., NAGIB, H.M. & HITES, M.H. 2000 A note on the overlap region in turbulent boundary layers. *Phys. Fluids* **12** (1), 1–4.

PANOFSKY, H.A., TENNEKES, H., LENSCHOW, D.H. & WYNGAARD, J.C. 1977 The characteristics of turbulent velocity components in the surface layer under convective conditions. *Boundary-Layer Meteorol.* **11** (3), 355–361.

PERRY, A.E. & ABELL, C.J. 1975 Scaling laws for pipe-flow turbulence. *J. Fluid Mech.* **67** (2), 257–271.

PERRY, A.E. & ABELL, C.J. 1977 Asymptotic similarity of turbulence structures in smooth- and rough-walled pipes. *J. Fluid Mech.* **79** (4), 785–799.

PERRY, A.E. & CHONG, D.M.S. 1982 On the mechanism of wall turbulence. *J. Fluid Mech.* **119**, 173–217.

PERRY, A.E., HENBEST, S. & CHONG, D.M.S. 1986 A theoretical and experimental study of wall turbulence. *J. Fluid Mech.* **165**, 163–199.

PERRY, A.E. & LI, J.D. 1990 Experimental support for the attached-eddy hypothesis in zero-pressure-gradient turbulent boundary layers. *J. Fluid Mech.* **218**, 405–438.

PERRY, A.E., LIM, K.L. & HENBEST, S.M. 1987 An experimental study of the turbulence structure in smooth- and rough-wall boundary layers. *J. Fluid Mech.* **177**, 437–466.

POND, S., SMITH, S.D., HAMBLIN, P.F. & BURLING, R.W. 1966 Spectra of velocity and temperature fluctuations in the atmospheric boundary layer over the sea. *J. Atmos. Sci.* **23** (4), 376–386.

PUCCIONI, M., CALAF, M., PARDYJAK, E.R., HOCH, S., MORRISON, T.J., PERELET, A. & IUNGO, G.V. 2023 Identification of the energy contributions associated with wall-attached eddies and very-large-scale motions in the near-neutral atmospheric surface layer through wind lidar measurements. *J. Fluid Mech.* **955**, A39.

SAMIE, M., MARUSIC, I., HUTCHINS, N., FU, M.K., FAN, Y., HULTMARK, M. & SMITS, A.J. 2018 Fully resolved measurements of turbulent boundary layer flows up to $Re_\tau = 20\,000$. *J. Fluid Mech.* **851**, 391–415.

SEIBERT, P., BEYRICH, F., GRYNING, S.-E., JOFFRE, S., RASMUSSEN, A. & TERCIER, P. 2000 Review and intercomparison of operational methods for the determination of the mixing height. *Atmos. Environ.* **34** (7), 1001–1027.

SMITS, A.J., MCKEON, B.J. & MARUSIC, I. 2011 High-Reynolds number wall turbulence. *Annu. Rev. Fluid Mech.* **43** (1), 353–375.

STIPERSKI, I. & CALAF, M. 2023 Generalizing Monin–Obukhov similarity theory (1954) for complex atmospheric turbulence. *Phys. Rev. Lett.* **130** (12), 124001.

TAYLOR, G.I. 1938 The spectrum of turbulence. *Proc. R. Soc. Lond. A: Math. Phys. Sci.* **164** (919), 476–490.

TOWNSEND, A.A.R. 1976 *The Structure of Turbulent Shear Flow*. Cambridge University Press.

TURAN, O., AZAD, R.S. & KASSAB, S.Z. 1987 Experimental and theoretical evaluation of the k^{-1} spectral law. *Phys. Fluids* **30** (11), 3463–3474.

WANG, G. & ZHENG, X. 2016 Very large scale motions in the atmospheric surface layer: a field investigation. *J. Fluid Mech.* **802**, 464–489.

WELCH, P. 1967 The use of fast Fourier transform for the estimation of power spectra: a method based on time averaging over short, modified periodograms. *IEEE Trans. Signal Process.* **15** (2), 70–73.

WILCZAK, J.M., ONCLEY, S.P. & STAGE, S.A. 2001 Sonic anemometer tilt correction algorithms. *Boundary-Layer Meteorol.* **99** (1), 127–150.

WILSON, J.D. 2008 Monin–Obukhov functions for standard deviations of velocity. *Boundary-Layer Meteorol.* **129** (3), 353–369.

WINKEL, E.S., CUTBIRTH, J.M., CECCIO, S.L., PERLIN, M. & DOWLING, D.R. 2012 Turbulence profiles from a smooth flat-plate turbulent boundary layer at high Reynolds number. *Expl Therm. Fluid Sci.* **40**, 140–149.

WYNGAARD, J.C. 1988 Structure of the PBL. In *Lectures On Air-Pollution Modeling* (ed. A. VENKATRAM & J.C. WYNGAARD), pp. 9–61. American Meteorological Society.

WYNGAARD, J.C. 1992 Atmospheric turbulence. *Annu. Rev. Fluid Mech.* **24** (1), 205–234.

YANG, H. & BO, T. 2018 Scaling of wall-normal turbulence intensity and vertical eddy structures in the atmospheric surface layer. *Boundary-Layer Meteorol.* **166** (2), 199–216.

ZILITINKEVICH, S.S. 1972 On the determination of the height of the Ekman boundary layer. *Boundary-Layer Meteorol.* **3** (2), 141–145.